

## CHAPTER 3

### STRUCTURE AND EVOLUTION OF THE INTRASEASONAL OSCILLATION



*”Surely in meteorology the thing to hunt down is a cycle, and if that is not to be found in the temperate zone, then go to the frigid zones and look for it, or the torrid zones and look for it, and if found, then above all things, and in whatever manner, lay hold of it, study it, record it, and see what it means.”*

— J.N. Lockyer, upon learning of sunspot cycles, 1871

#### 3.1 Theories for Summertime ISO Evolution

Figure 1.7 shows clear observational evidence of a northward (and southward) movement of convection during northern summer. The presence of these large-scale northward propagating systems and their link to active and break periods of rainfall over India has been known for a long time, as outlined in Section 1.2.1. The northward propagation along an individual meridian appears also to be connected to eastward propagation of convection, both along the equator and along Indian subcontinent latitudes. It will be shown that this eastward movement at Indian subcontinent latitudes is a persistent feature of the summertime ISO and therefore any theory accounting for the northward movement of convection should also

account for the observed eastward movement of convection both along the equator and Indian subcontinent latitudes.

A number of theories have been put forth that attempt to explain the observed northward propagation of convection. Webster (1983) and Srinivasan *et al.* (1993) emphasized the important role of land surface heat fluxes into the boundary layer that destabilize the atmosphere ahead of the ascending zone, causing a northward shift of convective activity. Goswami and Shukla (1984) suggested that the northward propagation is due to a convection-thermal relaxation feedback wherein the convective activity increases static stability while dynamic and radiative relaxation decreases the moist static stability, bringing the atmosphere to a convectively unstable state. Lau and Peng (1990), in a modeling study, find that the interaction between the large-scale monsoon flow and the equatorial intraseasonal oscillation results in the generation of unstable westward propagating baroclinic disturbances. As these disturbances grow, low-level air is drawn northward resulting in a rapid northward shift of the area of deep convection. Another interpretation of the northward propagation of convection is that the equatorial convection splits after it arrives in the central equatorial Indian Ocean with the bulk of the convection redirected northward and southward and the remainder continuing eastward into the western Pacific Ocean (Wang and Rui 1990). Under this view, the northward movement of convection is considered to be independent of the eastward propagation of convection along the equator and is thought to be initiated by different dynamical processes than those that are important to the evolution of the ISO. Recently, Rodwell (1997) hypothesized, supported by atmospheric model results, that breaks in the Indian monsoon can be triggered by injection of dry, high negative potential vorticity air from the Southern Hemisphere midlatitudes.

While the above theories may be important in determining the detailed characteristics of the northward propagation of convection, and hence the cycling of active and break periods, they fail to address, and cannot be readily extended to explain, either the concomitant southward movement of convection into the southern hemisphere or the eastward propagation of convection along Indian subcontinent latitudes. The theory most consistent with the observations shown in Fig. 1.7 is that of Wang and Xie (1997), who, based on results of a modeling study of the northern summer ISOs, describe the northward "propagation" as a convection "front" formed by the equatorial Rossby waves emanating from the equatorial convection. The Wang and Xie convection front tilts northwestward from the equator to 20°N, resulting in an apparent northward propagation as the entire wave packet migrates eastward.

It is interesting that, during winter, distinct poleward propagation of convection is essentially absent except for the occasional appearance of a south-eastward extension of convection into the South Pacific Convergence Zone (SPCZ) (e.g., Wang and Rui 1990). Matthews *et al.* (1996) show that the south-eastward extension is triggered by the equatorward advection of large magnitude potential vorticity (PV) air by the upper-tropospheric anticyclone centered over the equatorial convection. The high PV air induces deep ascent on its eastern side at a latitude of 15°–30°S, inducing convection in the SPCZ.

The goals of this chapter include examining the northward movement of convection with an emphasis on the role of propagating equatorial modes in driving the large-scale northward migrations of convection. To this end, it is useful to compare the evolution of the ISO during winter and summer since the winter ISO is slightly stronger and exhibits a less complicated evolution than its summertime

counterpart. A second goal is determining whether eastward propagation of convection along the equator, such as that observed in Fig. 1.7, is a prerequisite for northward propagation onto the South Asian landmass or whether an independent large-scale northward propagating mode that is not related to the ISO is also present during the summer Asian monsoon season.

### 3.2 Timeseries Analysis and Temporal and Spatial Filtering

#### 3.2.1 Fourier Spectral Analysis

In order to determine which regions in the tropics are influenced by oscillations in convection that are on the timescale of the ISO (25 to 80-days), a simple Fourier spectral analysis of daily OLR timeseries is completed at each grid point across the entire eastern hemisphere tropics. The analysis is conducted for northern summer and northern winter separately. Variance spectra at each individual grid point are completed for 182-day summer (MJJASO) and 182-day winter (NDJFMA) anomaly OLR timeseries. Prior to computing the variance spectra at each grid point, the mean and first three harmonics of the annual cycle are removed from the daily OLR timeseries. Additionally, the timeseries are tapered to zero with a 10% cosine taper to reduce the introduction of high-frequency variance generated by potentially unequal end values. An ensemble variance spectrum for northern summer and northern winter is determined by averaging the 22 individual summer and winter variance spectra, respectively.

OLR timeseries, like many geophysical timeseries, are assumed to exhibit red noise behavior which can be represented with a lag-1 autoregressive model:

$$x_n = \alpha x_{n-1} + z_n, \quad (3.1)$$

where  $\alpha$  is the lag-1 autocorrelation of the timeseries and  $z_n$  is Gaussian white noise. The discrete Fourier variance spectrum of the autoregressive model, as provided by

Gilman *et al.* (1963) is:

$$P_k = \frac{1 - \alpha^2}{1 + \alpha^2 - 2\alpha \cos 2\pi k/N}, \quad (3.2)$$

where  $k = 0 \dots N/2$  is the frequency index. The theoretical 90%, 95%, and 99% significance spectra can then be estimated by using the mean of the 22 lag-1 autocorrelations obtained from each seasonal timeseries and assuming 44 degrees of freedom (d.o.f., 22 years  $\times$  2).

The dynamical fields associated with the ISO exhibit a relatively narrow spectral peak between 50 and 60 days and are concentrated in wavenumber 1 (Salby and Hendon 1994). On the other hand, Salby and Hendon showed that the convective signal is considerably more broadband in both period (25 to 95 days), and wavenumber (1 to 3). Using these characteristics as a guide, Fig. 3.1a shows the areal extent in which a spectral peak between 25 and 80 days exceeds the 90%, 95%, and 99% theoretical significance spectra in northern summer and northern winter. The 80 day cutoff, rather than 95 days, is chosen to avoid identifying spectral peaks at low frequencies as ISO related when they may in fact be caused by linear trends in the OLR data. The simple requirement that only a single spectral peak between 25 and 80 days exceeds the theoretical spectrum is a liberal method of delineating regions that exhibit ISO-timescale convective activity. In both seasons, significant spectral peaks in the 25–80-day period band are observed across much of the tropical eastern hemisphere. The most clearly distinguishable difference between the two seasons is the extension of ISO-timescale activity northward over the Arabian Sea, the Indian subcontinent, and the South China Sea during the northern summer while ISO-timescale activity increases over the Java Sea and northern Australia during the northern winter.

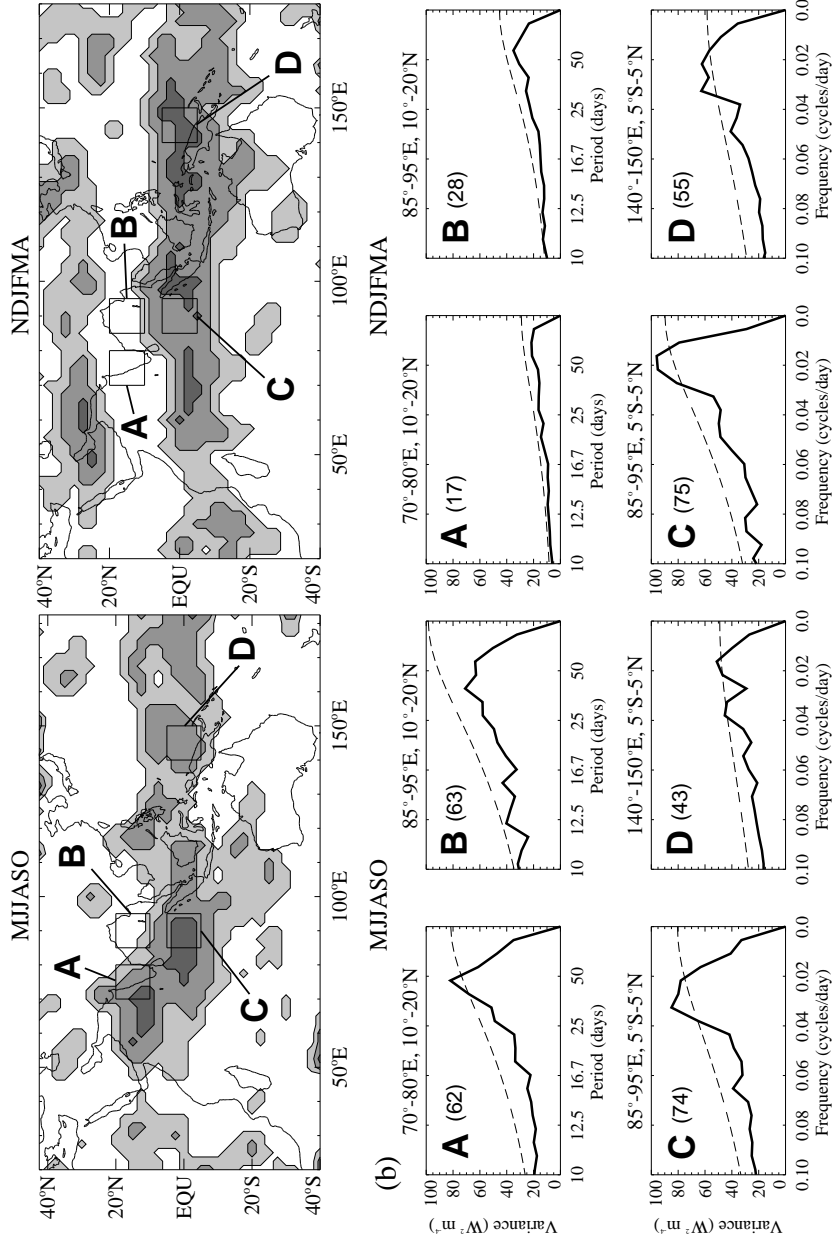


Figure 3.1. (a) Region in which a statistically significant spectral peak in OLR between 25 and 80 days is found in the ensemble variance spectra for the May–October summer and November–April winter seasons respectively. Progressively darker filled contours delineate regions in which a spectral peak between 25 and 80 days exceeds the 90%, 95%, and 99% significance levels, respectively, for a red-noise spectrum that is based on a lag-1 autocorrelation. (b) Examples of averaged ensemble variance spectra from selected regions as indicated by the enclosed boxes in (a). Dashed lines are the 95% significance level theoretical red-noise spectra. Values in parentheses are mean 25–80-day variance with units  $\text{W}^2 \text{ m}^{-4}$ .

Sample area-averaged ensemble variance spectra and the 90% theoretical red noise significance curves are shown in Fig. 3.1b for selected regions. A seasonal shift in the geographical distribution of ISO-timescale activity is clearly visible. The results shown in Fig. 3.1 are consistent with previous studies. For example, in a spectral analysis of a 70-year record of daily summertime precipitation from 3700 stations across India, Hartmann and Michelsen (1989) found a statistically significant 40–50-day spectral peak at the 99% level across the majority of the Indian subcontinent south of about 23°N.

### 3.2.2 Wavenumber-Frequency Analysis

Wavenumber-frequency spectral analysis is used to evaluate and to isolate the predominant spatial and temporal scales in the Asian monsoon region. This technique is useful for studying zonally propagating waves (Hayashi 1982) and has previously been employed to investigate convectively-coupled equatorial waves by Takayabu (1994) and Wheeler and Kiladis (1999) where the technique is described in detail. The wavenumber-frequency spectral variance is determined by

$$|F(m, \omega)|^2 = F(m, \omega)F^*(m, \omega), \quad (3.3)$$

where

$$F(m, \omega) = \frac{1}{2\pi T} \int_0^T dt \int_0^{2\pi} f(\lambda, t) e^{-i(m\lambda + \omega t)} d\lambda \quad (3.4)$$

and  $f(\lambda, t)$  is the original timeseries data at all longitudes ( $\lambda$ ) around an individual latitude line,  $m$  is the zonal wavenumber ( $2\pi/\lambda$ ),  $\omega$  is the frequency, and  $T$  is the length of the timeseries.

The results of a wavenumber-frequency spectral analysis of OLR are shown in Fig. 3.2. As with the Fourier spectral analysis described above, the plots in Fig. 3.2 represent an ensemble average of the 22 individual wavenumber-frequency spectra generated from 182-day segments. Prior to the wavenumber-frequency cal-

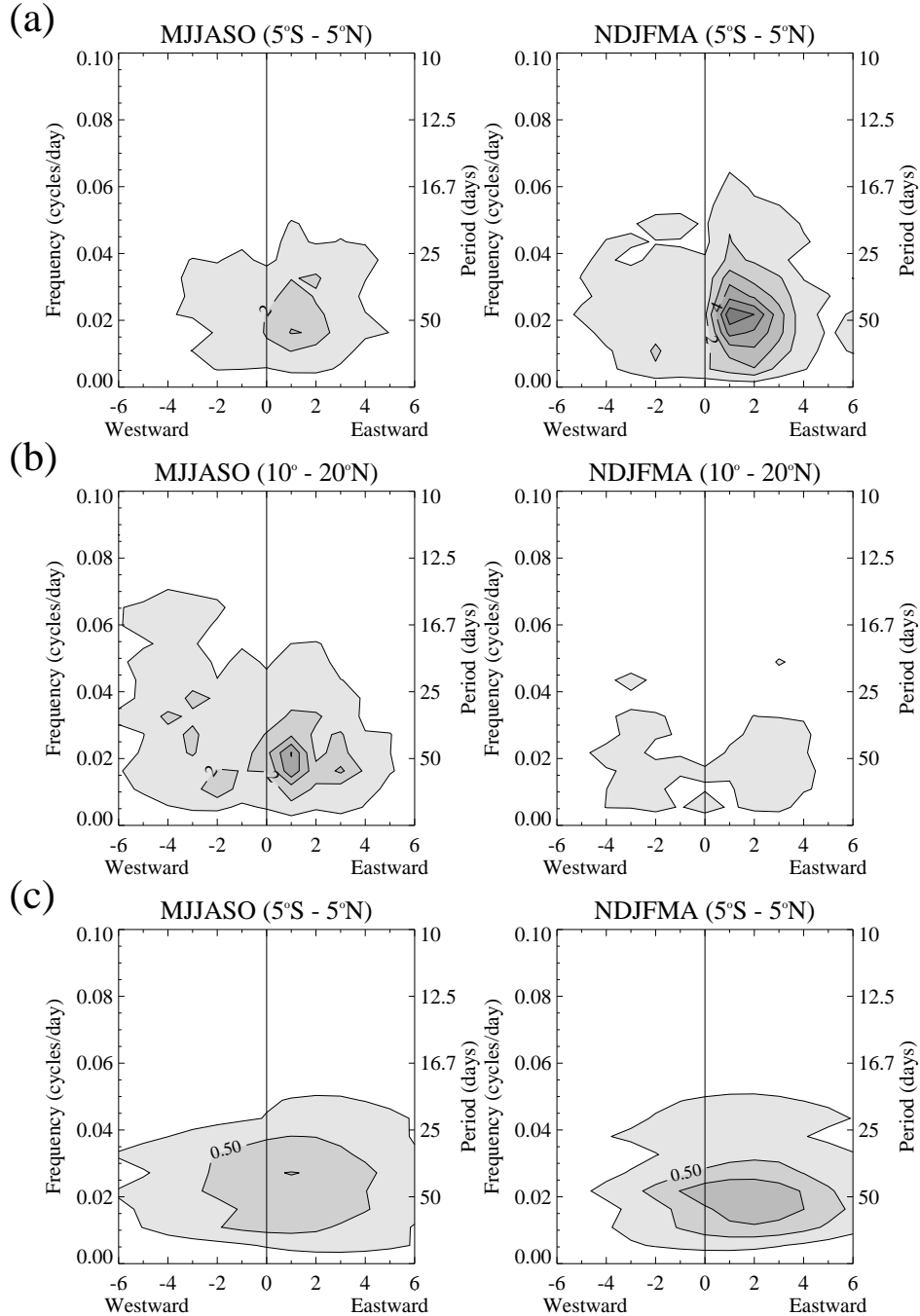


Figure 3.2. Average zonal wavenumber-frequency variance spectra of anomalous OLR for MJJASO and NDJFMA. The spectra are averaged over the number of summers and winters in the record and additionally are averaged across the latitudes (a)  $5^{\circ}\text{S}$  -  $5^{\circ}\text{N}$  and (b)  $10^{\circ}\text{N}$  -  $20^{\circ}\text{N}$ . (c) Same as (a) except wavenumber-frequency spectra calculated from data restricted to the longitudes  $40^{\circ}$ - $100^{\circ}\text{E}$ . Contours are every  $1\text{ W}^2 \text{ m}^{-4}$ .

culations, the mean, the first three harmonics of the annual cycle, and the linear trend are removed from each original 182-day OLR timeseries and the resulting anomaly timeseries is tapered to zero at the ends with a 10% cosine taper. Two longitude bands that extend around the entire globe are chosen for each season, a swath along the equator ( $5^{\circ}\text{S} - 5^{\circ}\text{N}$ , Fig. 3.2a) and a band that includes the Indian subcontinent and southeast Asia ( $10^{\circ} - 20^{\circ}\text{N}$ , Fig. 3.2b).

At equatorial latitudes there is a clear concentration of variance in eastward propagating modes, specifically at eastward wavenumbers 1–3 with periods greater than 25 days. This result is in accord with the findings of Salby and Hendon (1994) who observed that the variance at these wavenumbers and periods is notably greater in northern winter compared to northern summer. This observation has led, in general, to a greater emphasis on studies of the wintertime and springtime ISO. However, referring back to Fig. 3.1b, one sees that the regional mean variance between 25 and 80 days at  $85^{\circ} - 95^{\circ}\text{E}$ ,  $5^{\circ}\text{S} - 5^{\circ}\text{N}$ , for example, is basically the same during both summer and winter. Why then is the wavenumber-frequency spectral variance at eastward wavenumbers 1–3 so much greater during winter relative to summer (Fig. 3.2a)? One possible reason is suggested by Fig. 3.3 which shows the global distribution of seasonal mean 25–80-day OLR variance. The climatological 25–80-day OLR variance extends further east across the Pacific Ocean and is generally distributed closer to the equator during winter compared to summer. A wavenumber-frequency calculation done for the  $40^{\circ} - 100^{\circ}\text{E}$  longitudinal domain only results in a considerable reduction in the difference between summer and winter low-frequency, eastward-wavenumber variance (Fig. 3.2c).

Across South Asia the low-frequency, eastward-wavenumber 1–3 variance is substantially greater during summer than during winter (Fig. 3.2b). At this point,

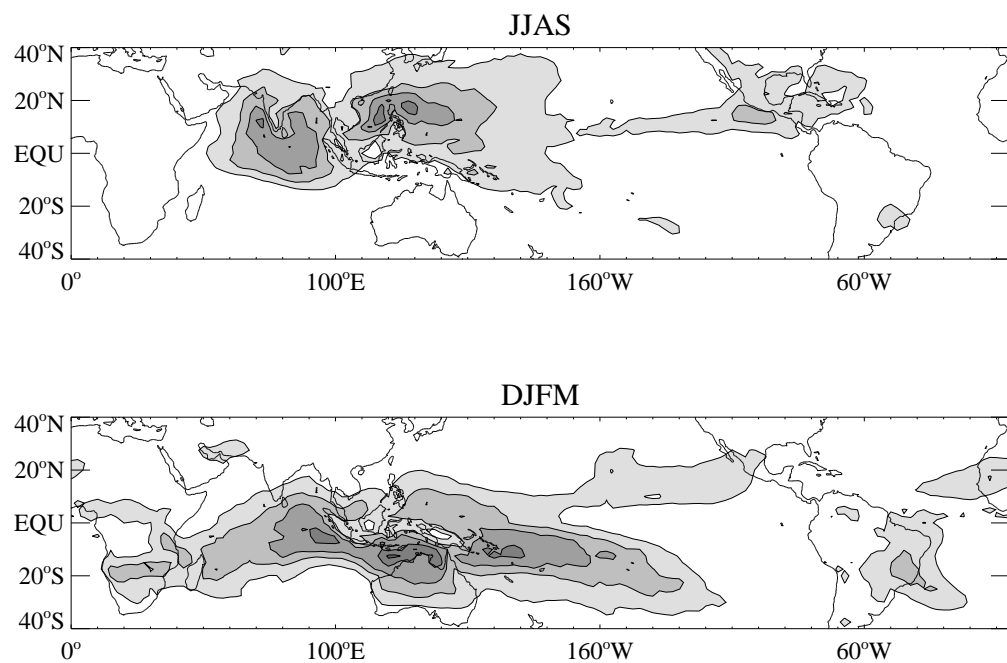


Figure 3.3. Climatology of 25–80-day OLR variance for JJAS and DJFM, contour levels every  $100 \text{ W}^2 \text{ m}^{-4}$ .

an important finding in this work is that while most of the literature describing the intraseasonal oscillations during the southwest monsoon has focused on the northward propagation of convection from the equator onto the Indian subcontinent, the wavenumber-frequency calculations indicate that there is also an eastward propagation of low-frequency convection both at the equator and along Indian subcontinent latitudes.

Wavenumber-frequency spectra of  $u_{200}$  and  $u_{1000}$  and 1000-mb divergence are shown in Fig. 3.4. In all three fields, wavenumber-frequency variance is concentrated at eastward wavenumber 1 during both seasons at a period of 50 days. However, the 1000-mb divergence spectrum appears to be much more evenly spread across all wavenumbers and frequencies. This is due, at least in part, to higher wavenumbers being emphasized when a spatial derivative is taken, as in the case of divergence. At  $10^{\circ}$ – $20^{\circ}$ N, the variance is similarly concentrated at eastward wavenumber 1 for all three fields, although the amplitude is much reduced for  $u_{1000}$  and 1000-mb divergence (not shown).

A comparison of Figs. 1.6 and 3.3 suggests that regions of climatological warm SST ( $\text{SST} \geq 28^{\circ}\text{C}$ ) tend to be collocated with high mean 25–80-day OLR variance. Figure 3.5 is a time-latitude diagram of the SST annual cycle with superimposed contours of 25–80-day, eastward-wavenumber-1–3-OLR variance, extending from  $20^{\circ}$ S to  $20^{\circ}$ N along both Arabian Sea and Bay of Bengal longitudes. Elevated OLR variance closely follows the migration of warm SSTs back and forth across the equator, generally at about a one month lag. In April and May, preceding the arrival of the Indian monsoon, the mean SST approaches  $30^{\circ}\text{C}$  in both the Arabian Sea and the Bay of Bengal. The warm SSTs in late spring are followed about a month later by high OLR variance that persists from late May through

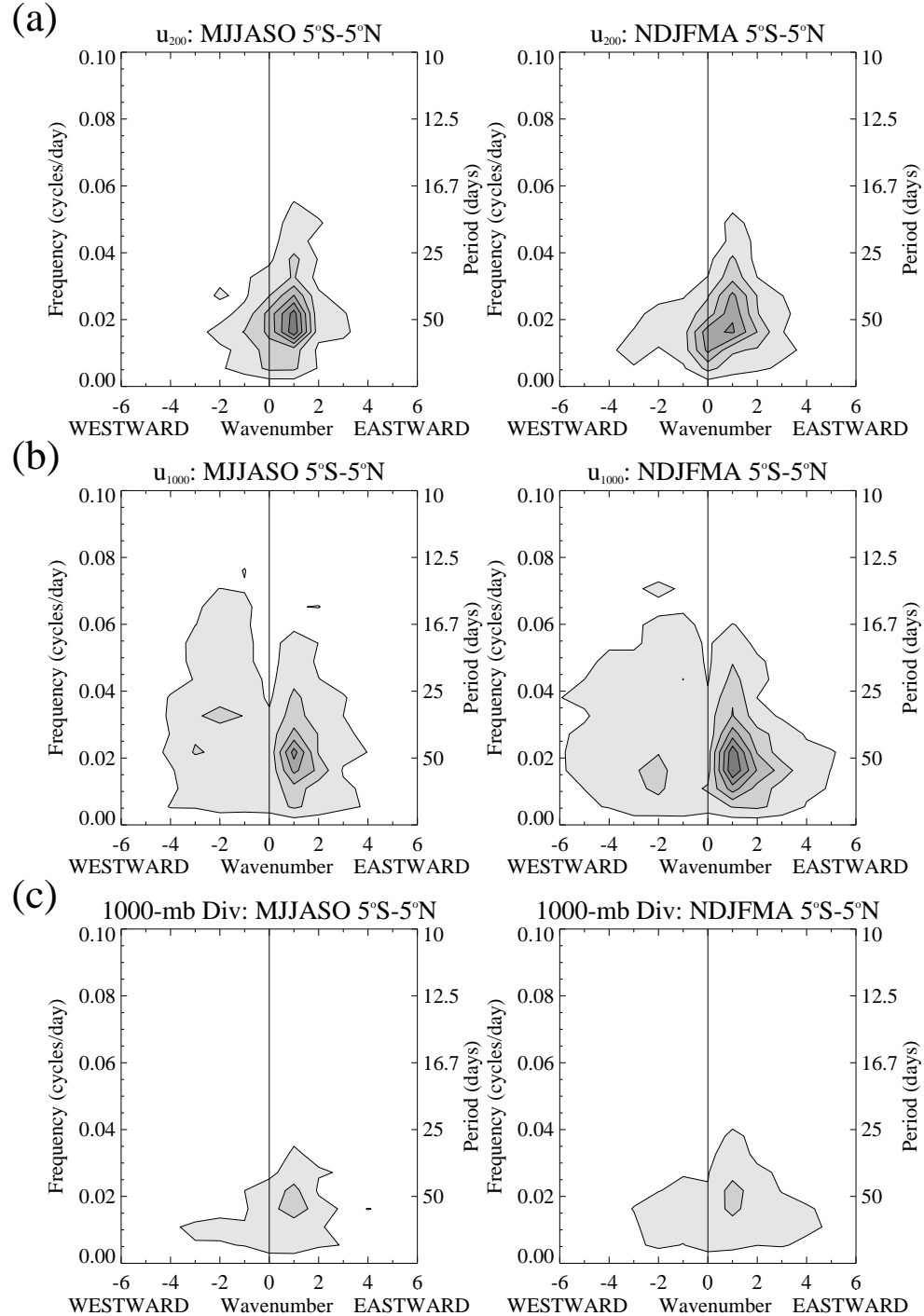


Figure 3.4. As in Fig. 3.2 except wavenumber-frequency variance spectra (expressed as percent of total variance) (a)  $u_{200}$ , (b)  $u_{1000}$ , and (c) 1000-mb divergence for MJASO and NDJFMA averaged across latitudes  $5^{\circ}\text{S} - 5^{\circ}\text{N}$ . Contour intervals are (a) 0.5%, (b) 0.2%, and (c) 0.1%.

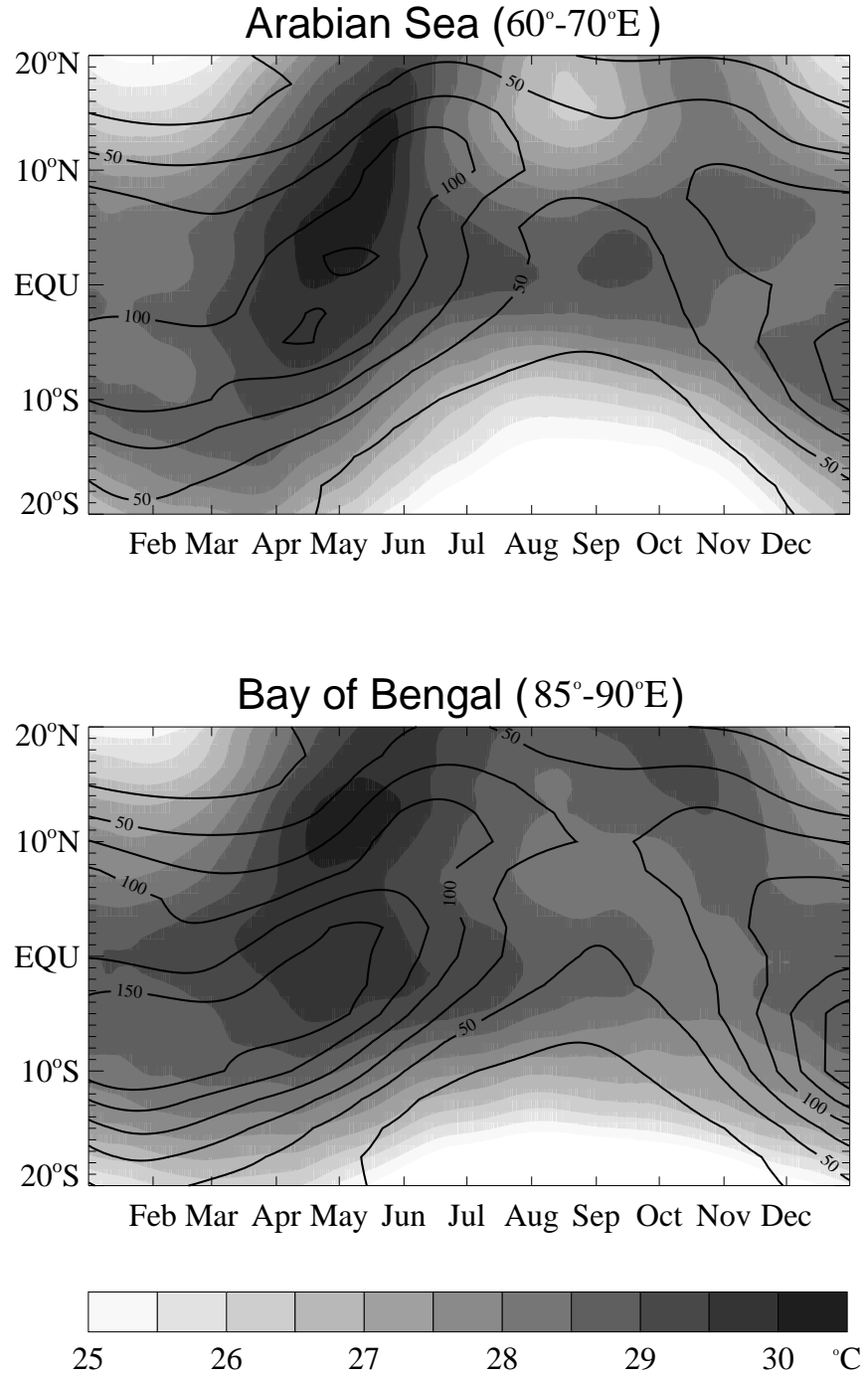


Figure 3.5. Time-latitude diagrams of annual cycle for SST (shaded) and 25–80-day, wavenumber-1–3-OLR variance (contours). Two sections are shown, one through the Arabian Sea ( $60^{\circ}$ – $70^{\circ}$ E) and one through the Bay of Bengal ( $85^{\circ}$ – $95^{\circ}$ E). Contour intervals are  $0.5^{\circ}\text{C}$  starting at  $25^{\circ}\text{C}$  for SST and  $25 \text{ W}^2 \text{ m}^{-4}$  starting at  $25 \text{ W}^2 \text{ m}^{-4}$  for OLR variance.

July. As the monsoon season progresses, the SST cools significantly in the Arabian Sea due to reduced solar flux, increased evaporation, advection of cold, upwelling water in the Somali current, and more vigorous mixing of the upper ocean. As the SST cools, the low-frequency OLR variance decreases, probably due to overall reduction in deep convection at all timescales (Grossman and Durran 1984; Grossman and Garcia 1990).

**3.2.3 Filtering** With the above spectral analysis in mind, the OLR and NCEP/NCAR data are filtered using two methods. First, a wavenumber-frequency filter is applied, retaining periods between 25 and 80 days as well as eastward wavenumbers 1–3 in the manner described by Wheeler and Kiladis (1999). The bandpass filtered data is used to compare the large scale features of the ISO between summer and winter and is denoted, henceforth, with a subscript 25–80<sub>e</sub> (e.g. OLR<sub>25–80<sub>e</sub></sub>) where "25–80" represents the timescale of filtration and the "<sub>e</sub>" represents the filtering of the data to retain eastward wavenumbers 1 to 3 only. The mean summer and winter variance in this wavenumber-frequency band is shown in Fig. 3.6. Since the greatest contribution of the OLR variance at periods 25 to 80 days is found at eastward wavenumbers 1 to 3, the OLR<sub>25–80<sub>e</sub></sub> variance appears as a smoothed version of the 25–80-day bandpass-filtered OLR variance shown in Fig. 3.3.

The second type of filter is a simple temporal bandpass Lanczos filter with 121 weights (see Duchon 1979), retaining periods between 25 and 80 days. The Lanczos filter is characterized by a sharp cutoff response and minimal Gibbs oscillation. Data filtered in this manner is denoted with a subscript "25–80" (e.g. OLR<sub>25–80</sub>) and is used to investigate the smaller scale (i.e. less than wavenumber 1–3) circulation and convection features associated with the northern summer

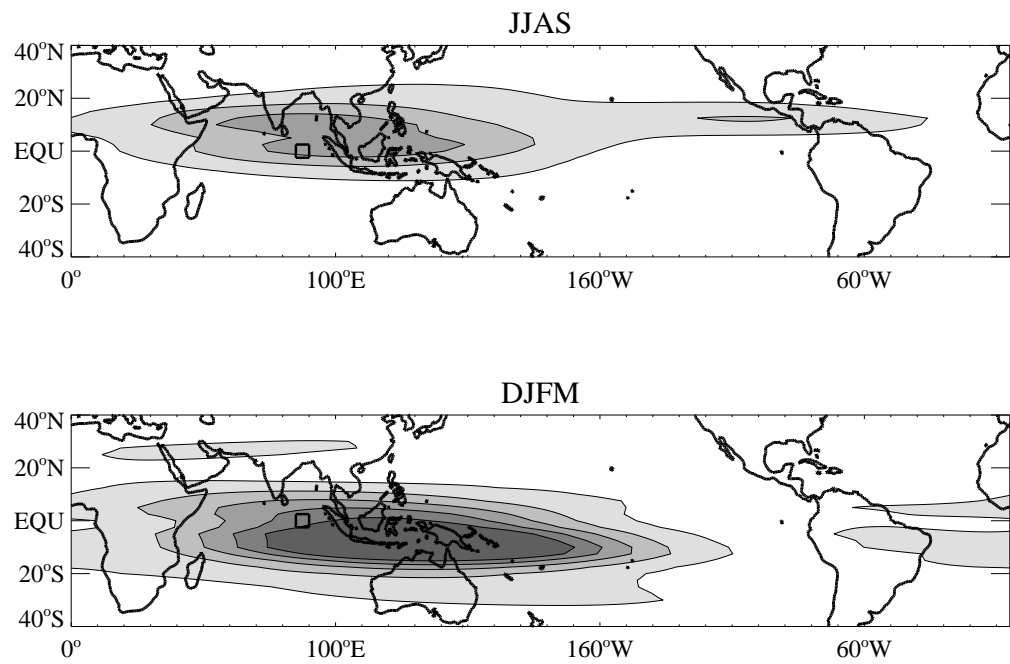


Figure 3.6. Climatology of 25–80-day period, eastward wavenumbers 1–3 OLR variance for JJAS and DJFM, contour levels every 25  $\text{W}^2 \text{ m}^{-4}$ . Box indicates region from which predictive timeseries is extracted for lagged cross-correlation and linear regression analysis completed in Sections 3.3 and 3.4.

ISO in the Indian Ocean basin. The mean and first three harmonics of the annual cycle are removed from the data prior to filtering.

### 3.3 Seasonal Structure of the Planetary Scale Intraseasonal Oscillation

To study the evolution of the large scale convection and circulation during a typical ISO cycle, the cross-correlation and linear regression technique described in Section 2.2.2 is employed using  $\text{OLR}_{25-80e}$  as the predictor. A  $5^\circ$  longitude by  $5^\circ$  latitude area in the central equatorial Indian Ocean ( $85^\circ\text{--}90^\circ\text{E}$ ,  $2.5^\circ\text{S}\text{--}2.5^\circ\text{N}$ ) is chosen as the base region. The selection of this location, while not entirely objective, is based on the observation that this region's low-frequency climatological  $\text{OLR}_{25-80e}$  variance is high and roughly equivalent during both seasons (see boxed region in Fig. 3.6). The standard deviation of  $\text{OLR}_{25-80e}$  in the base region is  $\sim 9 \text{ W m}^{-2}$  during summer and  $\sim 11 \text{ W m}^{-2}$  during winter. The difference in standard deviation between seasons appears to be due more to fewer occurrences of large amplitude convective events during summer rather than a reduced amplitude of convective events themselves (not shown). Since the lagged cross-correlation and linear regression technique maps the global amplitude of regressed convection and circulation based on a single standard deviation of OLR in a base region, a smaller standard deviation in summer will result in smaller amplitudes of regressed circulation and convection anomalies everywhere. Therefore, to facilitate the comparison between seasons of the response to equivalent convection anomalies, the summer standard deviation of  $\text{OLR}_{25-80e}$  in the base region is scaled to match that in winter.

In Hendon and Salby (1994), regression equations are developed solely based on time periods when a discrete intraseasonal signal in OLR, bandpass filtered to eastward wavenumbers 1–3 and 35–95-day periods, is present at  $85^\circ\text{E}$ ,  $0^\circ\text{N}$  (for details, see the companion study Salby and Hendon 1994). The method of

windowing they used selects episodes of activity that occur primarily during the period December to May when the discrete signal in convection at the equator is strongest. The primary difference between this work and that of Hendon and Salby is that, instead of selecting only episodes of discrete ISO activity, the stratification is purely according to season without regard to the presence or absence of a statistically significant ISO signal. The potential drawback of this method is that non-discrete episodes of eastward propagation are included in the regression equations. However, as will be shown, the results for the winter season closely match those of Hendon and Salby (1994) indicating that a careful selection of discrete events is not required. This is likely due to a domination of the regressions by the discrete events that fall within each season.

Figures 3.7, 3.8, and 3.9 display maps of the lagged cross-correlation and linear regressions for summer (left panels) and winter (right panels) for OLR in addition to the 200-mb wind and streamfunction, the 850-mb wind and divergence, and the 1000-mb wind and divergence, respectively.

The winter maps strongly resemble the more general results of Hendon and Salby (1994), as one would expect since the December to March winter period largely overlaps the December to May period when the discrete signal in ISO convection is strongest at the equator. The life cycle of the winter and spring ISO in convection, circulation, and divergence is described in detail in Hendon and Salby's paper, consequently, only the salient points that are important in the context of comparison with the life cycle of the summer ISO are discussed here.

It is important to stress that the maps shown here represent the lagged relationships between equatorial OLR<sub>25–80°e</sub> and identically filtered wind fields. There

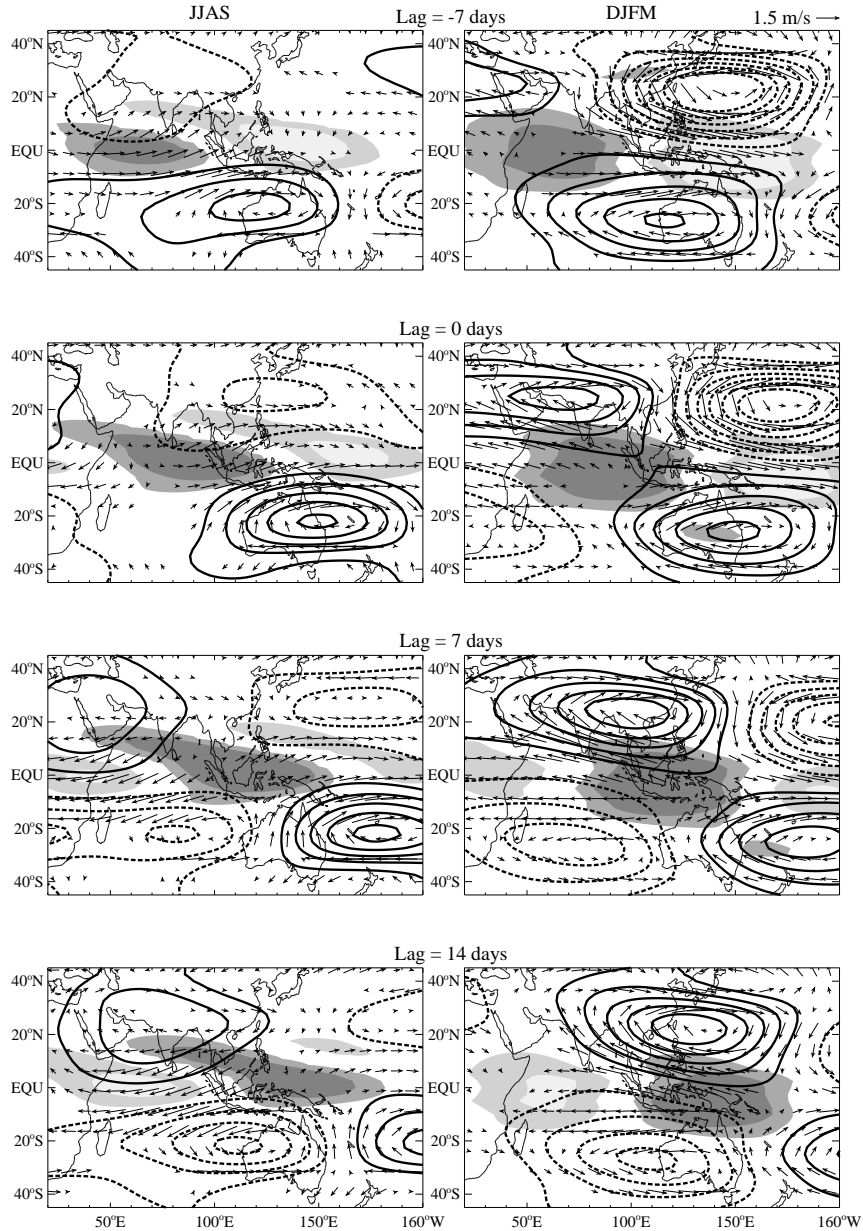


Figure 3.7. OLR (shaded), 200-mb wind (vectors), and 200-mb streamfunction (contours) perturbations associated with a  $-1\sigma$  deviation in  $\text{OLR}_{25-80e}$  in the base region;  $85^{\circ}\text{--}90^{\circ}\text{E}$ ,  $2.5^{\circ}\text{S}\text{--}2.5^{\circ}\text{N}$ . All data are bandpass filtered to eastward wavenumbers 1–3 with 25–80-day periods. Lagged regressions for JJAS (left) and DJFM (right) between  $-7$  and  $+14$  days every 7 days are shown. Only locally significant OLR and wind vectors are plotted. Shading levels for OLR levels are every  $4 \text{ W m}^{-2}$ , with dark shades indicating negative OLR anomalies and light colors indicating positive OLR anomalies. Streamfunction contour interval is  $7.5 \times 10^5 \text{ m}^2 \text{ s}^{-1}$  with the zero contour omitted.

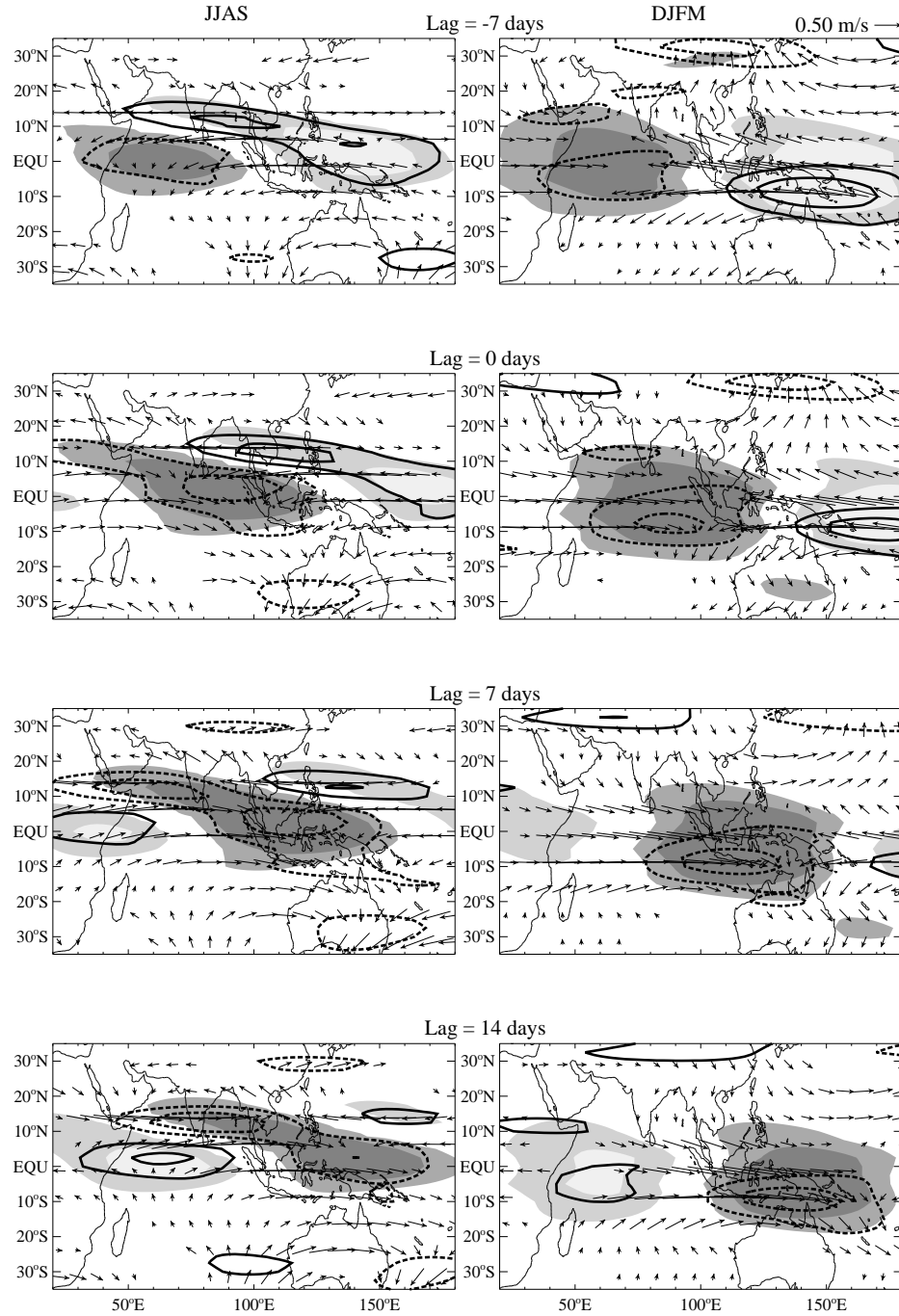


Figure 3.8. Same as Fig. 3.7 except for OLR (shaded), 850-mb wind (vectors), and 850-mb divergence (contours). Shading as in Fig. 3.7. Dashed lined contours indicate convergence and solid lines indicate divergence with a contour interval of  $1 \times 10^{-7} s^{-1}$  with the zero contour omitted.

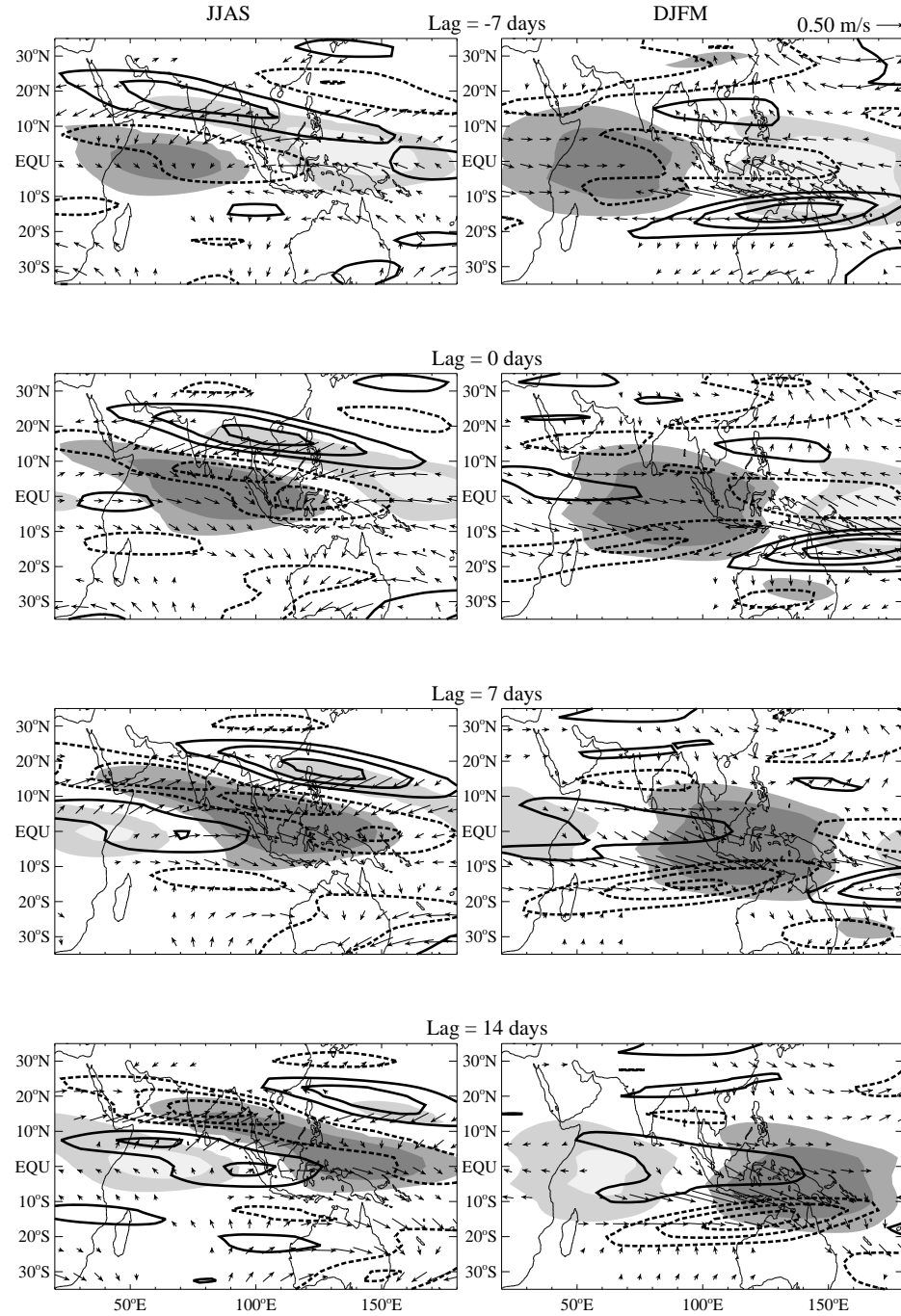


Figure 3.9. Same as Fig. 3.7 except for OLR (shaded), 1000-mb wind (vectors), and 1000-mb divergence (contours). Shading as in Fig. 3.7. Dashed lined contours indicate convergence, solid lines indicate divergence with a contour interval of  $1.5 \times 10^{-7} s^{-1}$  with the zero contour omitted.

is no a priori reason to assume that the total response to large-scale equatorial convection would be restricted to large-scale eastward propagating features. However, since the wavenumber-frequency variance is concentrated at eastward wavenumbers 1 to 3 in OLR, winds, and divergence (Figs. 3.2 and 3.4), one would anticipate that the total response to large-scale convection in winds and convection would be dominated by large-scale eastward propagating anomalies. In any case, the method used in this section appears to efficiently isolate the large-scale features of the summertime and wintertime ISOs. Lagged regressions against unfiltered OLR and winds which capture the smaller scale responses to large-scale equatorial convection will be shown in Section 3.4.

**3.3.1 Convection** The life cycle of convection relative to the summer and winter ISO is shown by the shaded contours in Figs. 3.7, 3.8, and 3.9. During winter, the convective signal straddles the equator with the center of convection located south of the equator by about  $5^{\circ}$  of latitude (Fig. 3.10). From Figs. 3.7-3.9, at lag  $-7$  days a convective anomaly is apparent in the western Indian Ocean from which point and time it steadily propagates eastward. As noted by Hendon and Salby (1994), the retention of only eastward wavenumbers 1–3 acts to smooth and stretch the regressed fields considerably. Here, this smoothing is manifested as a continuous east-west distribution of anomalous convection. The anomaly is even seen across the maritime continent, a region where the ISO signal in convection is generally weak in comparison to the stronger observed signals in the Indian Ocean and western Pacific Ocean.

During summer, the convective ISO signal evolves in a somewhat different manner. The sequence begins, as it does during wintertime, with an anomalous

region of convection in the western Indian Ocean at lag  $-7$  days. The latitudinal extent of the anomalous convection is more limited, though, to about  $10^{\circ}\text{S}$  to  $10^{\circ}\text{N}$  and is centered just north of the equator at  $2.5^{\circ}\text{N}$  (Fig. 3.10). The anomalous convective signal moves eastward along the equator, as it does during wintertime, but, beginning at lag 0 days, there is a northwestwardly oriented convective tail that extends to about  $20^{\circ}\text{N}$ . As the equatorial convection moves eastward, the off-equatorial tail shifts with it, moving across peninsular India by lag  $+7$  and lag  $+14$  days. The result, if one was observing along a single longitude, is the apparent northward propagation of convection from the central equatorial Indian Ocean to peninsular India. This perspective is shown in Fig. 3.11 as shaded contours along  $90^{\circ}\text{E}$  as a function of time. Consequently, referring to the shift in convection from the equator northward as a “northward propagation” does not reflect that the northward movement is actually a derivative of the northwestward orientation of convection in conjunction with the ISO’s eastward progression.

At a rate of about  $1^{\circ}$  latitude per day, it requires about 15-20 days for the convection to reach its northernmost extent at  $20^{\circ}\text{N}$ . At the time of the most-northward location of Indian monsoon domain convection, the equatorial convection is situated at  $150^{\circ}$ – $160^{\circ}\text{E}$ . The total anomalous convection pattern extends across nearly  $100^{\circ}$  of longitude (about 10,000 km) oriented along a southeast to northwest line. The longitudinal extent of the convection, though, is probably exaggerated due to stretching caused by the wavenumber filtering. In particular, the regressed signals in convection that appear over Saudi Arabia and the western Arabian Sea, regions that exhibit little organized convective activity during the summer monsoon, are almost certainly an artifact of using wavenumber filtered data. A more realistic

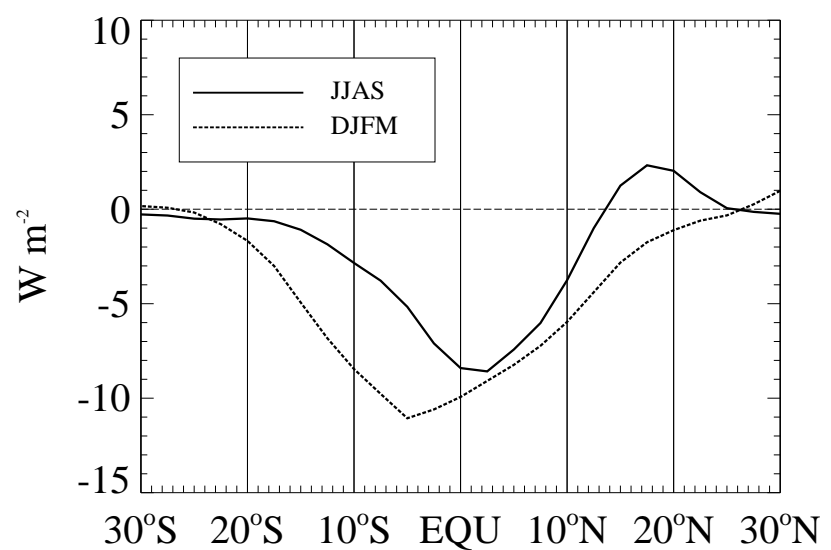


Figure 3.10. Regressed OLR versus latitude at lag zero days at 80°E. Solid line is JJAS and dashed line is DJFM.

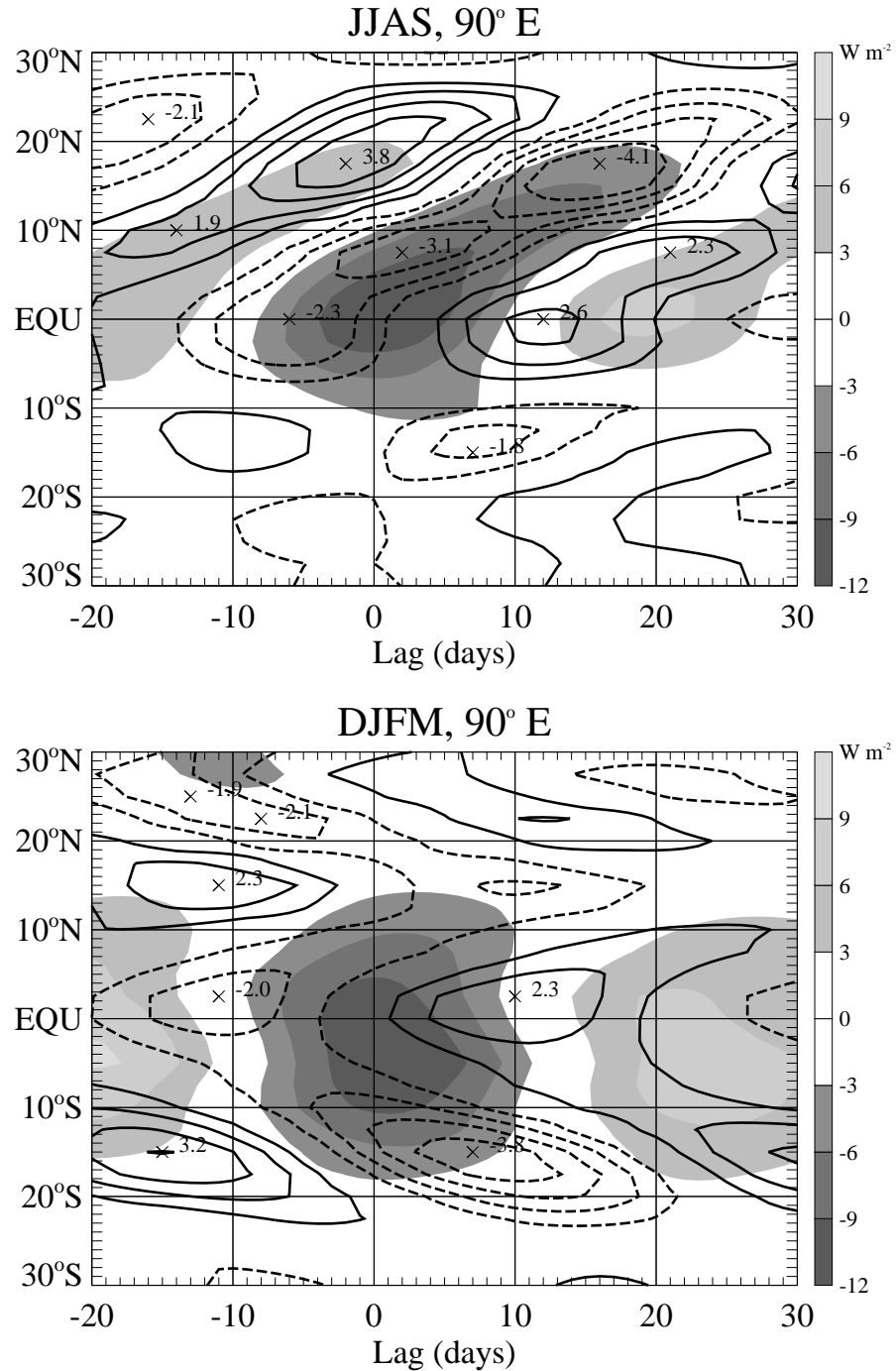


Figure 3.11. Lag-latitude diagrams along  $90^\circ\text{E}$  of regressed OLR (shaded) and 1000-mb divergence (contours). Divergence contour interval is  $1 \times 10^{-7} \text{ s}^{-1}$  with the zero contour omitted. Dashed lines indicate negative divergence or convergence. Central maxima and minima represent divergence multiplied by  $10^6$ .

representation of the evolution of ISO convection is shown in Section 3.4. Nevertheless, it seems that the active and break periods over India are part of a much larger scale oscillation that extends across the whole of the Asian monsoon domain.

### 3.3.2 Circulation

The wind vectors in Figs. 3.7, 3.8, and 3.9 represent the anomalous winds that have a statistically significant relationship to central equatorial Indian Ocean OLR<sub>25–80e</sub>. During winter (Fig. 3.7, right panels), large scale cyclonic and anti-cyclonic gyres dominate the 200 mb anomalous circulation patterns. Cyclonic gyres flank the equator west of the suppressed convection and anti-cyclonic gyres are located to the west of enhanced convection. These upper level gyres have been observed in a number of previous studies (e.g., Weickmann *et al.* 1985; Madden 1986; Hendon and Salby 1994) and resemble the Rossby wave response to imposed equatorial heating (Webster 1972; Gill 1980; Sardeshmukh and Hoskins 1988). Using a simple model showed (Gill 1980) calculated the low-level tropical circulation response to equatorial heating (Fig. 3.12a) which exhibits Rossby cells in either hemisphere to the west of the heat source in addition to Kelvin wave structure to the east of the heat source. Since the ISO convection in winter (and hence the latent heating) is centered roughly about the equator, the Rossby wave response is nearly symmetric about the equator with Rossby cells of approximately equal amplitude positioned at 25° latitude in either hemisphere. Sardeshmukh and Hoskins (1988) showed that an upper level steady divergence source (i.e. a heat source) on the equator will generate downstream Rossby cells of the opposite sign to the east of the divergence source in addition to those located to the west of the divergence source as predicted by the Gill model. Such downstream upper level gyres are seen in Fig. 3.7. However, since the regression analysis is a linear analysis, it is unclear whether or not the downstream Rossby cells are due to

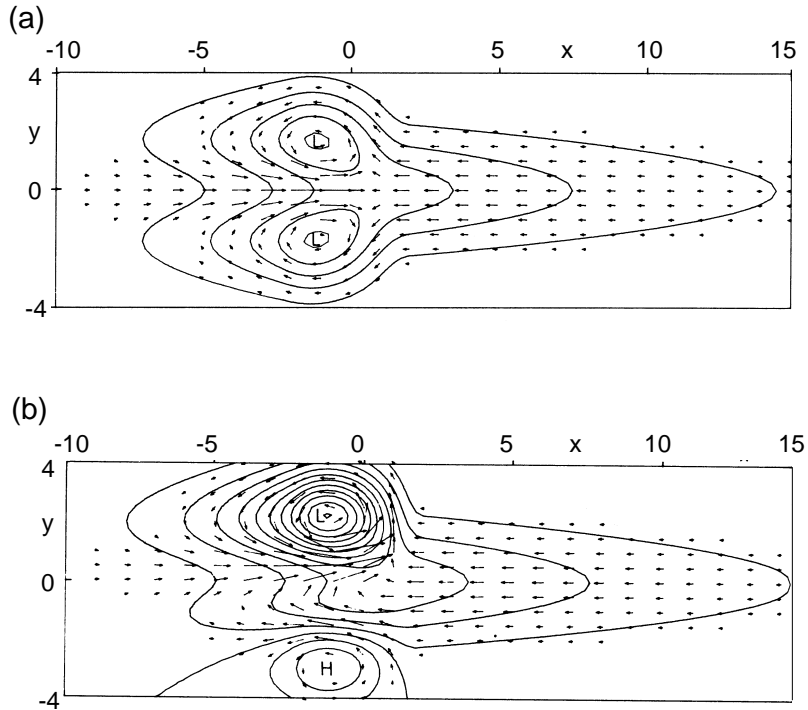


Figure 3.12. (a) Solution for lower layer velocity field for heating symmetric about the equator in region  $|x| < 2$ . Contours are perturbation pressure (contour interval 0.3) which is everywhere negative. (b) Same as (a) except solution for heating concentrated in northern hemisphere at  $|x| < 2$ . Figure adapted from Figs. 1 and 2, Gill (1980).

processes such as those outlined in Sardeshmukh and Hoskins (1988) or whether they are the linear response to the suppressed convection located about  $80^{\circ}$ – $90^{\circ}$  to the east of the enhanced convection.

During summer, the upper level Rossby gyres are not as clearly defined or as strong as during winter (Fig. 3.7, left panels). This lack of definition is probably due to the more complex northern summer ISO convection distribution which contains both the equatorial convection and the northwestward oriented off-equatorial band of convection. Consequently, a direct comparison of the regressed circulation features to the Gill model is not possible since the circulation response to the equatorial heat source is superimposed by the circulation response to the off-equatorial heat source. The problem of a complicated heat source in summer emphasizes the utility of comparing the summertime ISO evolution to that of the winter. The summertime and wintertime regressions are qualitatively similar which suggests that if the summertime ISO convection did not exhibit off-equatorial convection the circulation would resemble that of northern winter; that is, the ISO can be thought of in terms of the propagating equatorial waves predicted by the Gill model, regardless of season.

Structure that resembles a Kelvin wave is visible at 850- and 1000-mb in both seasons as anomalous easterlies to the east of the convection anomaly (Figs. 3.8 and 3.9). This result lends support to the theory that the summer ISO is not a unique mode of variability, but a modified ISO which is characterized by a Kelvin-Rossby wave packet response to equatorial heating. Convergence maxima are collocated with OLR anomalies at 850-mb in both seasons. At 1000-mb convergence maxima at the equator are displaced to the east of the convective anomaly. The convergence maxima at the equator have been ascribed to frictionally dominated convergence of

the Kelvin component easterlies onto the equator in the boundary layer (Wang and Rui 1990). The leading convergence may promote the steady eastward propagation of the ISO and is present during both seasons;  $50^{\circ}$ – $60^{\circ}$  to the east in winter and  $30^{\circ}$ – $40^{\circ}$  to the east during summer, although the exact displacement of convergence is unclear because of the effects of the heavy wavenumber-frequency filtering that is applied to the wind fields.

The surface convergence at the equator is flanked by convergence centers off the equator and about  $40^{\circ}$ – $80^{\circ}$  to the west of the equatorial convergence maxima. The off-equatorial convergence maxima are caused by frictional convergence in the viscous boundary layer into the surface lows that are found at the centers of the Rossby gyres, as predicted by Gill's model. The low pressure areas have a westward tilted structure with latitude that is mirrored in the surface convergence seen in Fig. 3.9. While both sides of the equator exhibit these off-equatorial convergence centers, the summer hemisphere convergence is notably stronger; that is, the stronger convergence is north of the equator in boreal summer and south of the equator in austral summer. The anti-symmetry between hemispheres is clearly visible during both seasons in Fig. 3.11 where the regressed 1000-mb divergence is contoured on top of the regressed OLR anomalies in a time-latitude diagram. The surface convergence exhibits a V-type structure in both seasons with notably stronger off-equatorial convergence located in the summer hemisphere.

Why is the off-equatorial convergence stronger in the summer hemisphere? One possible reason is that the equatorial ISO convection is not perfectly symmetric about the equator during either season (Fig. 3.10). The simple response to symmetric equatorial heating shown by (Gill 1980) (Fig. 3.12a) is not a complete description when the heat source is not symmetric about the equator. In a

separate experiment, Gill examined the circulation associated with heating that is focused in one hemisphere (Fig. 3.12b). He found that the Rossby cell located in the hemisphere that contains the strongest heating is amplified considerably which would lead in turn to stronger surface convergence into the center of that Rossby cell. Additionally, Gill found that there is significant cross-equatorial flow to the west of the heat source into the hemisphere that contains the heat source (Fig. 3.12b). Fig. 3.13 shows a time-longitude diagram of regressed OLR overlaid with  $v_{1000}$  contours. During summer, anomalous southerlies propagate eastward, lagging slightly the eastward moving equatorial convection. The southerlies lie to the west of the convection or the heat source and indicate low-level flow, consistent with Gill's anti-symmetric heating experiment, into the hemisphere that contains the preponderance of the heating. The opposite is true during winter with anomalous northerlies lagging west of the equatorial convection. The cross-equatorial flow into the summer hemisphere appears to strengthen the convergence within the Rossby cells in the summer hemisphere.

In summer, the off-equatorial convergence anomaly north of the equator leads the convection anomaly by about 3–5 days, implying that the convection advances northward into the region of off-equatorial surface convergence, in much the same way that the equatorial convection maintains its eastward propagation by shifting into the equatorial surface convergence. In winter, despite the reasonably strong off-equatorial surface convergence at 20°S that is oriented northeast-southwest, no analogous poleward propagation of convection is observed. The differences between the summertime ISO characteristics when northward propagation of convection is prominent and the wintertime ISO behavior when no southward propagation is evident may be linked to the dissimilar, and not simply opposite, climatological base

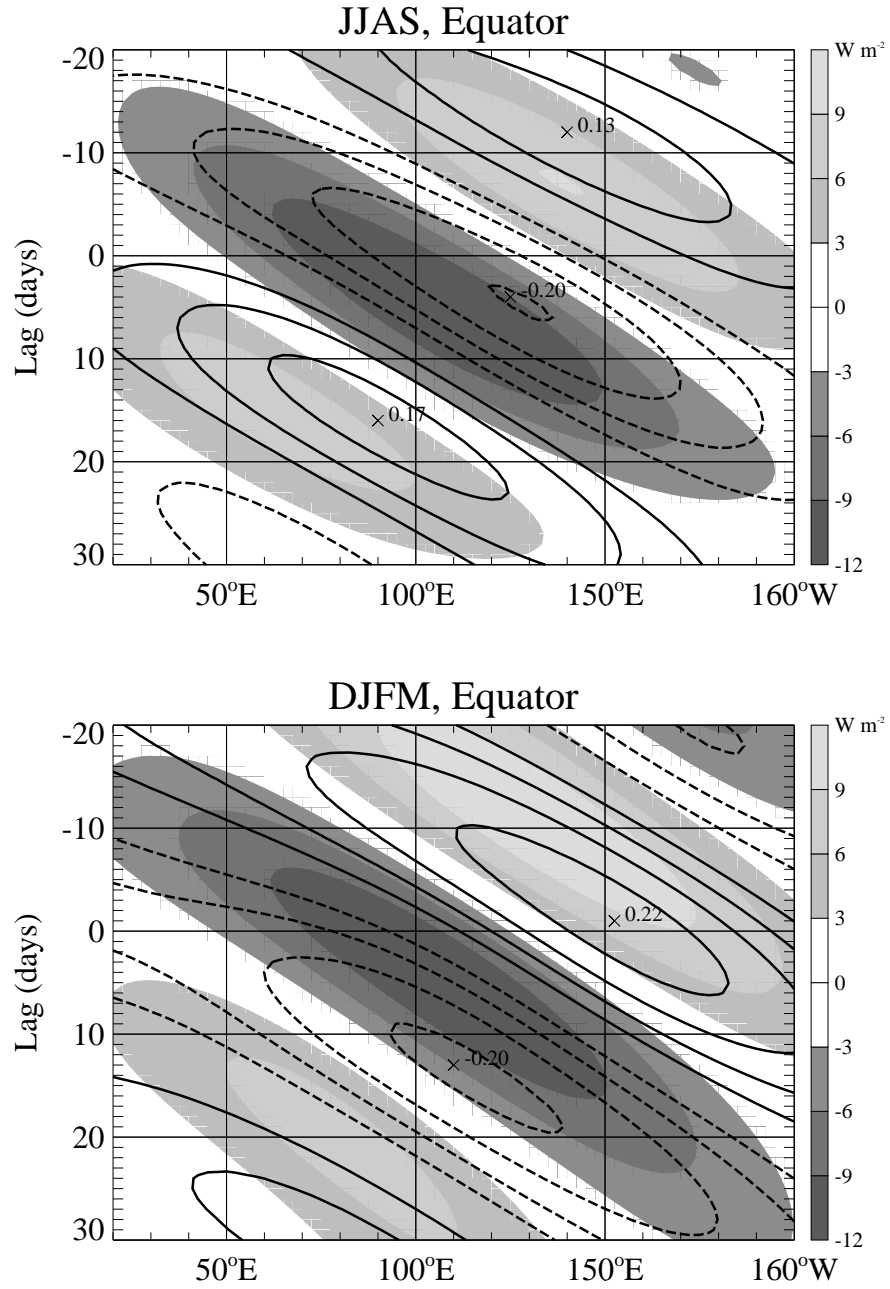


Figure 3.13. Lag-longitude diagram along equator of regressed OLR (shaded) and  $v_{1000}$  (contours). Meridional wind contour interval is  $0.05 \text{ m s}^{-1}$  with the zero contour omitted. Solid lines indicate southerly wind anomalies and dashed lines indicate northerly anomalies. Central maxima and minima of regressed  $v_{1000}$  values are denoted by x's.

states between seasons; that is, the winter climatological base state is not simply a reflection about the equator of the summer climatological base state.

Among the most obvious and definitive differences between the summertime and wintertime basic states are the warm SST distribution (Fig. 1.6) and the low-level monsoonal flow (Fig. 1.3). During winter, mean SSTs greater than 28°C extend south to about 10°–15°S across the Indian Ocean basin whereas during summer, warm SSTs envelop the entire northern Indian Ocean waters, including all of the Bay of Bengal and a sizeable fraction of the Arabian Sea. Therefore, since deep convection tends to develop in regions of warm SST (a necessary but not sufficient condition for deep convection) and is suppressed over areas of cool SST, no southward propagation into the convergence center is observed in northern winter. The low-level flow may also be a factor. During summer, the southwesterly flow into the Asian monsoon region transports moisture from the southern hemisphere and the Arabian Sea, fueling the monsoon rainfall (Cadet and Greco 1987; Fasullo and Webster 1999a). The winter monsoon flow is not as well developed and does not extend as far south as its summer counterpart, leaving the area of off-equatorial convergence located at 15°S without a steady external source of water vapor.

In summary, the overwhelming evidence of similar wave-like processes in the summer and winter ISOs suggests that they are the result of similar dynamical processes. The different evolutions of convection appear to be due primarily to the different base states between the seasons. In particular the warm SSTs and associated moist boundary layer extends significantly further to the north during boreal summer causing the whole of the northern Indian Ocean region to be conditionally unstable. Large-scale surface convergence into the Rossby cell in the conditionally

unstable region appears to initiate off-equatorial convection thereby generating a northwestward oriented band of convection. In the following section, the smaller scale circulation anomalies associated with the large-scale summertime ISO convection are examined.

### 3.4 Detailed Structure of the Summer Intraseasonal Oscillation

In this section, the summertime ISO is investigated in more detail with an emphasis on the variability between individual events. The results of a cross-correlation and linear regression analysis where the base region timeseries (summertime OLR<sub>25–80e</sub> in the central equatorial Indian Ocean as before) is regressed against unfiltered OLR,  $u_{200}$ ,  $v_{200}$ ,  $u_{850}$ , and  $v_{850}$  are shown as lagged regression maps in Figs. 3.14 and 3.15. Regressing against unfiltered data permits the visualization of the lagged convective signal that includes both higher wavenumbers (i.e. smaller horizontal scale features) and westward wavenumbers that were previously excluded. The evolution of the ISO in convection appears similar to before; that is, as the equatorial convection propagates to the east, the northwestward tilting band of convection moves with it, generating an apparent northward propagation of convection when viewed along any individual meridian. At the 200-mb level (Fig. 3.14), the westerlies to the east of the equatorial convection are a persistent feature in addition to cross-equatorial flow emanating from the convecting areas at days +6, +10, and +14. At 850-mb, the most prominent feature is the spin up or spin down of the mean monsoonal circulation (recall Fig. 1.3) relative to the presence of enhanced or suppressed convection over the Indian subcontinent. In other words, during the enhanced ISO convection phase over India, the low-level circulation is stronger than average (e.g., the cross-equatorial low-level jet to the east of Somalia (Findlater 1969)). The off-equatorial convection leads the spin up of the monsoonal

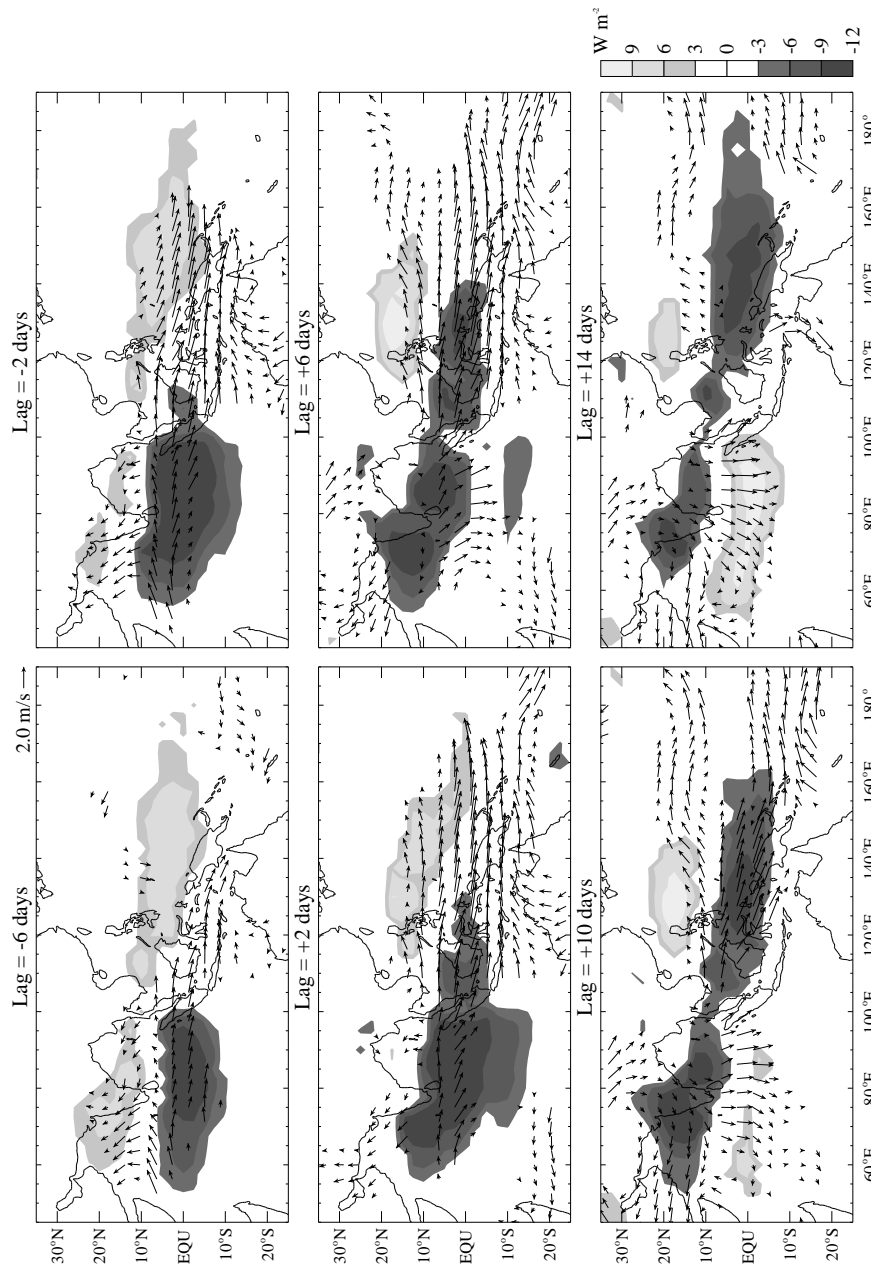


Figure 3.14. OLR (shaded) and 200-mb wind (vectors) perturbations associated with a  $1\sigma$  deviation in JJAS OLR<sub>25–80°e</sub> in the base region; 85°–90°E, 2.5°S–2.5°N. In contrast to Fig. 3.7, total anomaly fields (i.e., not filtered) are used in forming regressions. Only locally significant OLR and wind vectors are plotted.

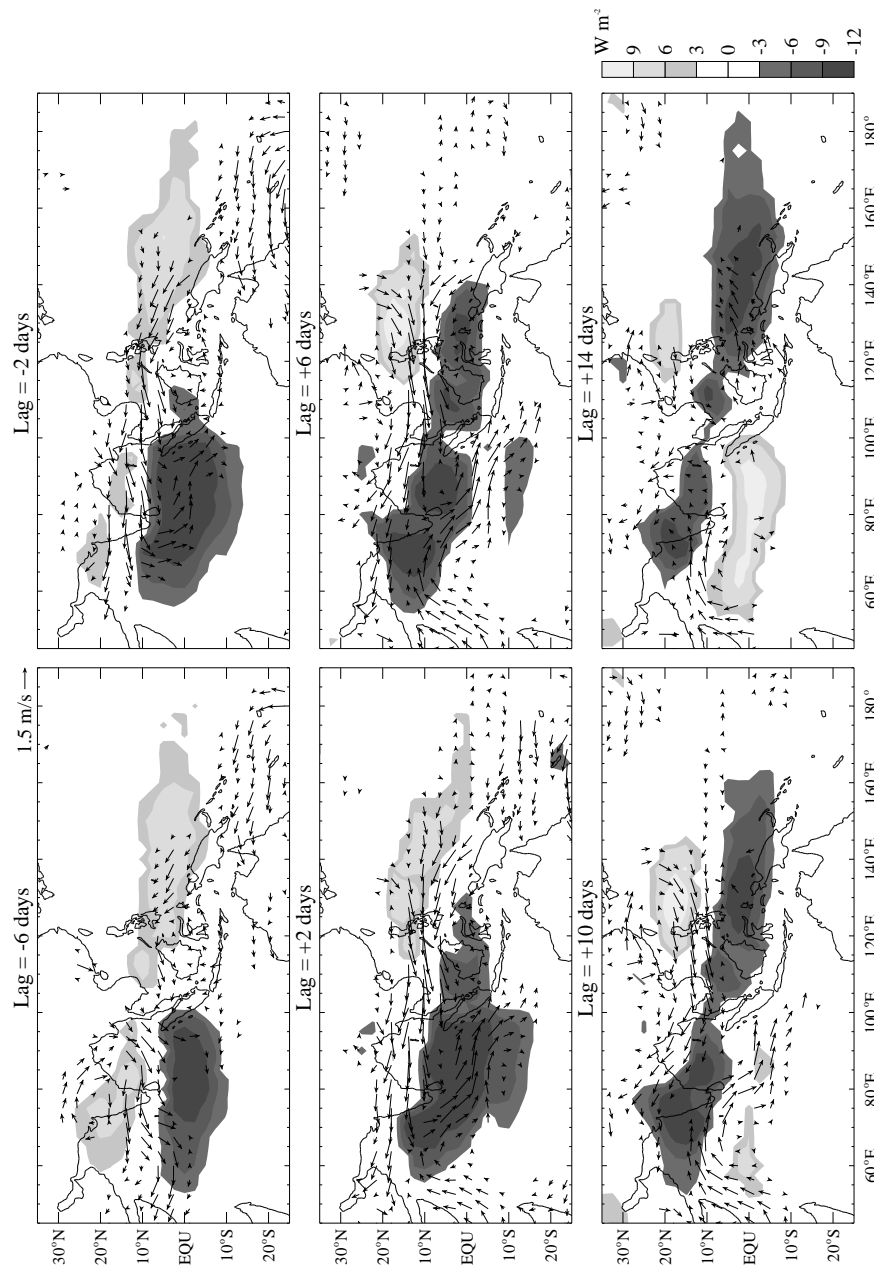


Figure 3.15: Same as Fig. 3.14 except for OLR and 850-mb wind.

circulation by a couple of days (not shown), indicating that the stronger monsoonal flow is a response to the off-equatorial convection.

Time-latitude and time-longitude sections along a number of longitudes and latitudes in the Indian Ocean are shown in Fig. 3.16. The dominant feature of the time-latitude sections in Fig. 3.16a is the predominance of "northward" movement of convection at all longitudes across the Indian Ocean basin. The northward propagation is accompanied by eastward movement at 15°N (Fig. 3.16b) which supports the view made in the previous section that the northward movement of convection is an artifact of the eastward movement of a northwestward oriented band of convection. An additional characteristic of the ISO convection, observed at 75°E and 90°E, that is absent in regressions with temporally and spatially filtered datasets is a southward movement of convection from the equator to about 10°–15°S (Fig. 3.16a). This anomalous convection center appears to propagate eastward as well, although the time-longitude diagram along 10°S (Fig. 3.16b) does not show this conclusively. The convection south of the equator is collocated with the area of off-equatorial convergence into the center of the southern hemisphere Rossby cyclone (Fig. 3.9, lag +7 days). This southern hemisphere convective anomaly does not appear in regressions of OLR<sub>25–80e</sub> presumably because it is of relatively short longitudinal extent and therefore high wavenumber. The southward propagating convective anomaly also overlies the climatological maxima in summer precipitation south of the equator (Fig. 1.4). The convection coincides with the southern off-equatorial convergence center generated by the southern Rossby cell of the Kelvin-Rossby wave packet and lies over relatively warm mean SSTs in excess of 28°C that extend to 10°S at Bay of Bengal latitudes throughout most of the summer (Fig. 3.5). Further west in the Indian Ocean, despite the fact that southern hemisphere off-equatorial convergence is

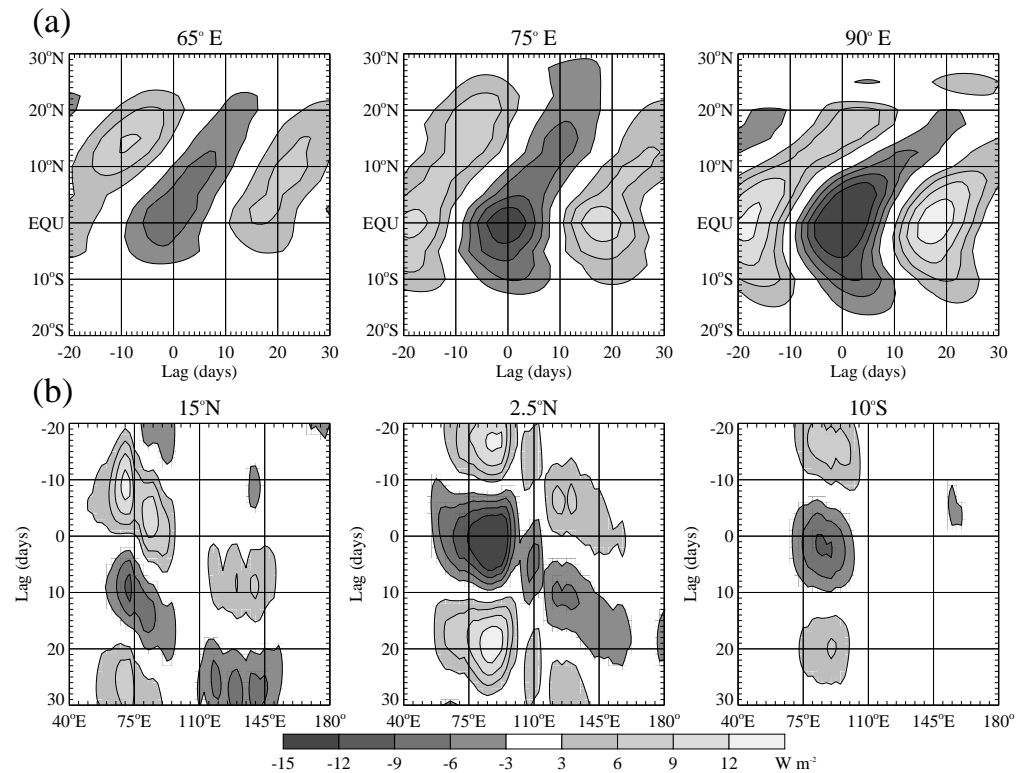


Figure 3.16. (a) Lag-latitude diagrams of regressed OLR<sub>25–80</sub> along 65°E, 80°E, and 90°E. (b) Lag-longitude diagrams of regressed OLR<sub>25–80</sub> along 15°N, 2.5°N, and 10°S.

observed during summer, no such southern hemisphere summer precipitation maxima or corresponding 25–80-day convection anomaly exists. Here, though, SSTs in excess of 28°C are confined to areas north of 5°S and hence deep convection is not supported in the area of off-equatorial convergence in the western Indian Ocean.

There is a suggestion in Fig. 3.16a that the poleward propagation speed varies across the Indian Ocean basin. The northward propagation rate is faster at a speed of about 1.5° per day in the Arabian Sea and over the Indian subcontinent compared to a speed of about 1° per day in the Bay of Bengal. The reduction in speed of northward propagation, as the ISO moves from west to east, could be a consequence of a reduction in the speed of propagation of the equatorial convection as it crosses the maritime continent. However, the time-longitude section along 2.5°N (Fig. 3.16b) does not provide definitive supporting evidence of such a change in phase speed along the equator. Another possibility is that the variation in northward speed across individual longitudes could be due to local feedbacks. Over the Indian subcontinent, once the convection anomaly reaches about 10°– 15°N it rapidly extends polewards to the base of the Himalayan mountains near 30°N. The notable change in phase speed as the convection crosses land suggests the influence of land surface feedbacks. Webster (1983) found that poleward movement of low-frequency convection over land can be explained by a sequence that starts with sensible heat input from the warm land surface into the boundary layer ahead of the convective zone. The sensible heat input destabilizes the atmosphere ahead of the convection followed by poleward encroachment of convection into the destabilized region. This poleward movement is aided by the reduction in sensible heat input equatorward of the convection by the evaporative cooling of the precipitation moistened ground. While this hypothesis could be reasonably advanced to explain

the rapid extension of convection northward to the Himalayas, it is a difficult theory to prove empirically because of a lack of available historical soil moisture data. In summary, the changes in northward propagation speed with longitude and latitude are not readily explained with the tools and data available in this study.

The biggest difference between the OLR<sub>25–80</sub> and OLR<sub>25–80e</sub> regressions is evident in Fig. 3.16b. At 2.5°N, the convection anomaly develops in place across much of the Indian Ocean basin beginning at lag –8 days, shortly after the convective anomaly first appears at 60°E at lag –10 days. This apparently stationary development of the convective anomaly, followed 10–20 days later by development of convection over India, has lead some authors to characterize the summer intraseasonal oscillation as an independent northward propagation event that is forced by entirely different dynamics than those important to the evolution of the ISO (e.g., Wang and Rui 1990). Since the cross-correlation and linear regression technique employed here is tantamount to compositing based on OLR<sub>25–80e</sub> or OLR<sub>25–80</sub> minimums, it is possible that two or more entirely different modes are wrapped up in the regression results. For example, one summer mode may be the typical eastward propagating ISO disturbance that has an associated northward propagating feature. This mode would be extracted by wavenumber-frequency filtering to eastward wavenumbers. The second mode could be a standing oscillation that develops in the equatorial Indian Ocean and moves northward over India independent of any eastward propagation of convection along the equator. Added together, these two modes would be sufficient to explain the time-longitude sections in Fig. 3.16, in which both stationary and eastward propagation, in addition to an apparent northward propagation, are seen.

**3.4.1 Separation of Modes** One way to approach the problem of separating the modes, if such a separation is appropriate, is to ask whether or not eastward propagation of convection along the equator is a prerequisite for a subsequent convection anomaly to move northward onto the Indian subcontinent and into the north Indian Ocean. To evaluate this hypothesis, the large-scale intraseasonal oscillation events are separated into those that are dominated by eastward propagation and those that can be characterized as a standing oscillation in the Indian Ocean basin. Fifty-six total large-scale intraseasonal oscillations in convection are cataloged by identifying summertime minimums in area-averaged OLR<sub>25–80e</sub> ( $85^{\circ}$ – $90^{\circ}$ E,  $2.5^{\circ}$ S– $2.5^{\circ}$ N) whose value is less than one standard deviation below the OLR<sub>25–80e</sub> mean ( $< -9 \text{ W m}^{-2}$ ). Fifty-six events over 22 summers translates to approximately 2.5 events per monsoon season. The identified dates of minimum OLR<sub>25–80e</sub> are then compared to the dates of minimums in OLR<sub>25–80w</sub> (wavenumber-frequency filtered OLR at periods 25–80 days and westward wavenumbers 1–3) for the same reference region. Minimums of OLR<sub>25–80w</sub> that occur within  $\pm 5$  days of a OLR<sub>25–80e</sub> minimum are tagged. Equal or nearly equal values for OLR<sub>25–80e</sub> and OLR<sub>25–80w</sub> imply a standing oscillation. That is,

$$OLRE_t \gg OLRW_{t\pm 5} \quad \rightarrow \quad E \text{ (eastward)} \quad (3.5)$$

$$OLRE_t \simeq OLRW_{t\pm 5} \quad \rightarrow \quad S \text{ (stationary)} \quad (3.6)$$

where  $OLRE$  and  $OLRW$  are the area-averaged OLR<sub>25–80e</sub> and OLR<sub>25–80w</sub> values, and  $t$  is the set of 56 dates of minimum  $OLRE$ .

Out of the initial pool of 56 large-scale eastward events, 23 (about 40%) also exhibit low OLR<sub>25–80w</sub> values. The 33 remaining events are characterized by a dominant eastward component. Instances where OLR<sub>25–80w</sub> is low, while OLR<sub>25–80e</sub> is not, are rare (occurring only three times) and are not considered here.

The identified large-scale equatorial convective events are further stratified according to whether or not northward propagation is evident in the days following a minimum in the equatorial convective signal. Clear northward propagation is apparent in 27 out of the 33 eastward events and 21 out of the 23 stationary events. The separation of events is summarized in Table 3.1. These results indicate that during the northern summer monsoon season, the majority of large-scale convective events at the equator are followed by a northward component indicating a clear link between the equatorial ISO and active and break periods of the monsoon. The question remains, however, whether or not eastward propagation of convection along the equator is required for there to be northward propagation of convection. The possibility exists that the large-scale convection events that exhibit stationary behavior in the equatorial Indian Ocean do not feature any eastward propagation and therefore represent a unique mode that may not be related to a Kelvin-Rossby wave packet response to equatorial convection.

Global OLR<sub>25–80</sub> is composited at lags between –30 days and +30 days based on the dates for eastward-northward (EN, 27 cases), stationary-northward (SN, 21 cases) events, and eastward-no northward (E, 6 cases) events. Figure 3.17 shows lag-latitude and lag-longitude diagrams of the resulting composites along 75°E (left panels) and 2.5°N (right panels). Focusing on the lag-longitude diagrams in the right panels one sees that, as expected, the EN events are characterized by steady eastward propagation along the equator from 60°E to the dateline. The SN events develop in place in the central equatorial Indian Ocean over the course of about 10–15 days. At lag +5 days, though, convective anomalies are seen at 120°E

Table 3.1. Mean characteristics of large-scale summertime ISO modes as defined in text and in Fig. 3.17.

Mode	EN	SN	E
Number of events	27	21	6
Number of events per season	1.2	1.1	0.3
Mean start date	Aug. 16	July 14	July 24
Mean minimum OLR <sub>25–80</sub> value (W m <sup>-2</sup> )	-17	-31	-23
Mean northward phase speed at 75°E (m s <sup>-1</sup> )	1.9	1.9	na
Mean northward phase speed at 90°E (m s <sup>-1</sup> )	1.3	1.4	na
Mean northern extent at 75°E	25°N	23°N	na

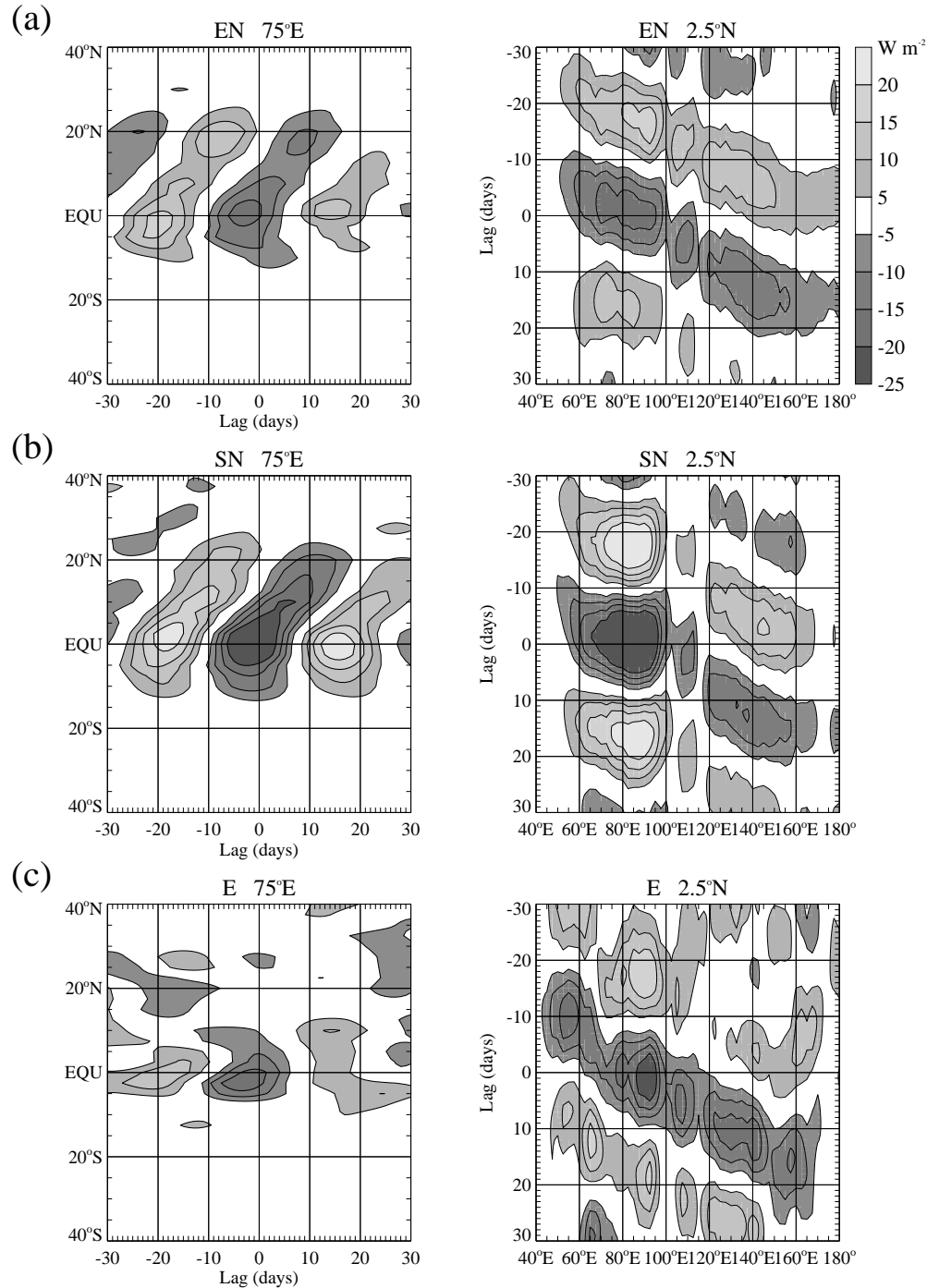


Figure 3.17. Lag-latitude along 75°E and lag-longitude along 2.5°N diagrams of composited OLR<sub>25-80</sub> segregated by intraseasonal convection event type as defined in text. EN corresponds to large-scale ISO events that exhibit eastward and northward movement, SN to stationary and northward movement, and E to eastward movement only. (a) EN events (27), (b) SN events (21), and (c) E events (6).

from which point the convection anomaly propagates steadily eastward to the date-line. At the same time, an apparent northward movement of negative OLR anomalies begins (see Fig. 3.17b left panel). This result implies that eastward propagation of convection along the equator is indeed a prerequisite for northward movement of convection into India.

To be certain that the SN composite is not being biased by a small number of large amplitude events, the individual SN events are separated according to whether or not convection anomalies in the central equatorial Indian Ocean are followed, within 5 to 25 days, by convection anomalies in the western equatorial Pacific Ocean ( $140^{\circ}$ – $150^{\circ}$ E). Out of the 21 SN events, only one is not followed by a conspicuous convection anomaly in the western equatorial Pacific Ocean. The observation that poleward propagation occurs only when accompanied by eastward propagation along the equator lends credence to the notion that the northward propagation, and hence the active and break cycles of the monsoon, are not the result of an independent and unique summertime mode, but are simply modified versions of the intraseasonal oscillation that is observed in winter.

The fundamental characteristics of each mode are summarized in Table 3.1. For the most part, the differences between the EN and SN northward propagating modes is small. The SN events appear to be somewhat stronger than the EN events with a mean minimum OLR<sub>25–80</sub> anomaly value in the base region of  $-31\text{ W m}^{-2}$  compared to  $-17\text{ W m}^{-2}$ . The northward movement speed and extent are essentially the same between modes.

Why does the equatorial convection sometimes develop simultaneously across the Indian Ocean basin and sometimes develop in the western Indian Ocean and propagate eastwards across the basin? Figure 3.18 is a histogram of the number

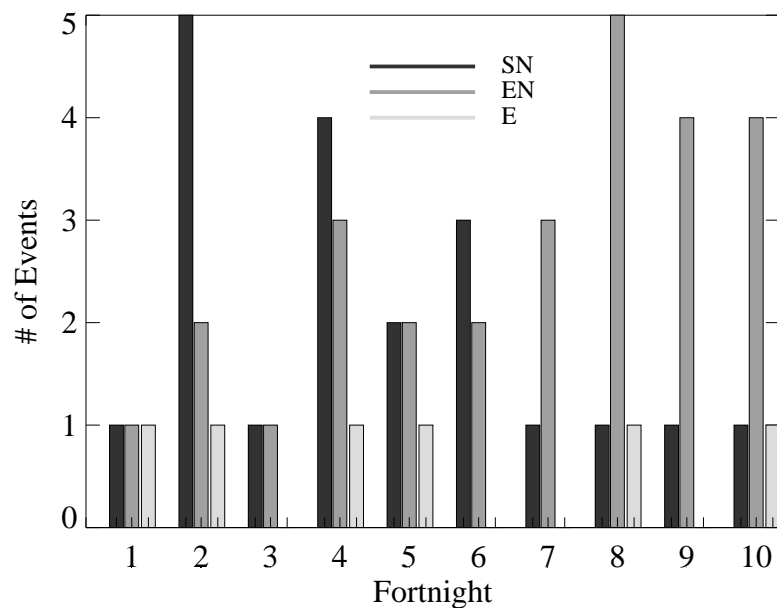


Figure 3.18. Histogram of the number of events (SN, EN, E as defined in the text and in Fig. 3.17) occurring in each of the 10 two-week periods that make up the monsoon season (May 15 to Sept 30).

of times the SN, EN, and E modes occur within each of the 10 two-week periods that span the summer monsoon season (May 15 to Sept. 30). The SN mode is strongly biased towards the beginning of the season, when the SSTs are at their warmest across the Indian Ocean basin. Almost equally sharply, the EN mode is biased towards the end of the season when the SSTs have cooled in the northern Indian Ocean. There is no indication that the relatively rare E events preferentially occur during any particular phase of the monsoon season. The relationship between SST and the occurrence of either the SN or EN modes is illustrated in Fig. 3.19 which is a difference map of composited mean SSTs averaged over lag -21 days to lag -7 days for the SN events minus the EN events. Mean SST differences in excess of  $0.5^{\circ}\text{C}$  are seen across the basin. Perhaps the basin wide warmer SST enhances instabilities in the boundary layer such that a large-scale convective disturbance originating in the western Indian Ocean rapidly spreads across the basin. As the convection develops across the basin, the Kelvin-Rossby wave packet response develops. Eventually, the Kelvin wave to the east of the convection amplifies to the point that equatorial convergence begins to draw the equatorial convection eastwards, initiating the apparent northward movement of convection at the same time. Later in the season when the SST has cooled across the basin (recall Fig. 3.5) and EN events become the dominant mode, the evolution of ISO events reverts to the "normal" sequence that begins with anomalous convection in the western Indian Ocean followed by a steady eastward propagation of convection that is driven by surface convergence onto the equator generated by the Kelvin wave response to the equatorial convection.

**3.4.2 Sea Surface Temperature** In recent years, speculation has increased that the ISO is a coupled air-sea mode of variability (e.g. Webster *et al.* 1998; Jones *et al.* 1998). Such a hypothesis is supported by Fig. 3.5, showing

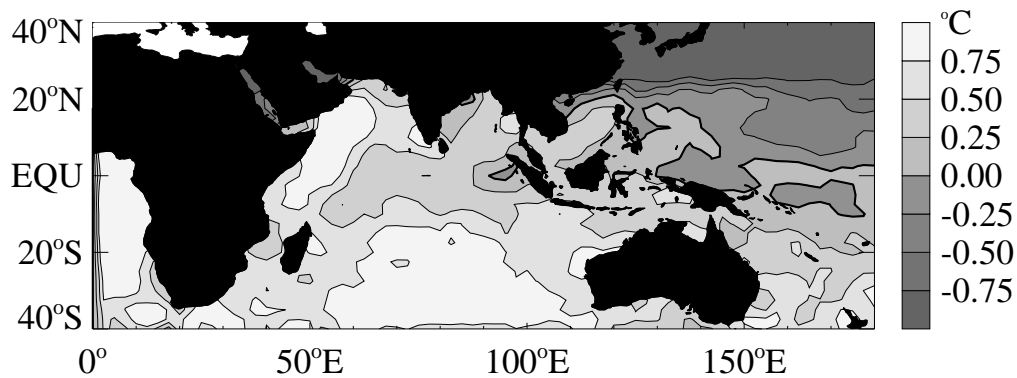


Figure 3.19. SST difference map of mean SST for SN – EN events. Mean SST for each type of event is determined by averaging SST between lag –21 days and lag –7 days to capture the basic state preceding the onset of equatorial convection. The zero contour is thickened for clarity.

the collocation of SST and OLR<sub>25–80</sub> variance, and Fig. 3.19, depicting the differences in mean SST preceding SN and EN events. Wang and Xie (1998) find in a modeling study that the warm pool basic states of the western Pacific and Indian Oceans with their deep thermoclines are conducive to intraseasonal timescale coupled variability. Shinoda *et al.* (1998) observe a 0.15°C amplitude variation in SST in the Indian Ocean that is associated with net surface heat flux variations of 30–40 W m<sup>-2</sup>. The net surface heat flux variations lead the SST variations by approximately one-quarter cycle. Fasullo and Webster (1999b) find that the surface heat flux variations are dominated by wind driven latent heat flux variations in addition to cloud-forced shortwave flux variations.

The results of a lagged composite of SST is shown in Fig. 3.20 where the central composite dates are the 15 SN event dates that occur during the period when weekly SST data is available (1982–1997). Daily SST estimates are generated by a linear interpolation between the weekly estimates. Prior to compositing, the mean and first 3 harmonics of the annual cycle are removed from the daily interpolated SST dataset. At lag –14 days, suppressed convection is positioned over the Arabian Sea and stretches across the southern tip of India and the southern Bay of Bengal. Anomalously warm SST with amplitudes reaching 0.15°C is located south of the area of suppressed convection. At lag –7 days, as the convection develops along the equator and the region of suppressed convection slides northward, the warm SST anomalies extend northward into the Arabian Sea. The warm SST anomaly is particularly strong along the coasts of Somalia and Saudi Arabia. Recalling the anomalous low-level circulation shown in Fig. 3.9, suppressed convection over India is accompanied by anomalous northeasterlies over the northwestern Indian Ocean, reducing the southwesterly monsoonal flow. Reduced monsoon surface winds could result in

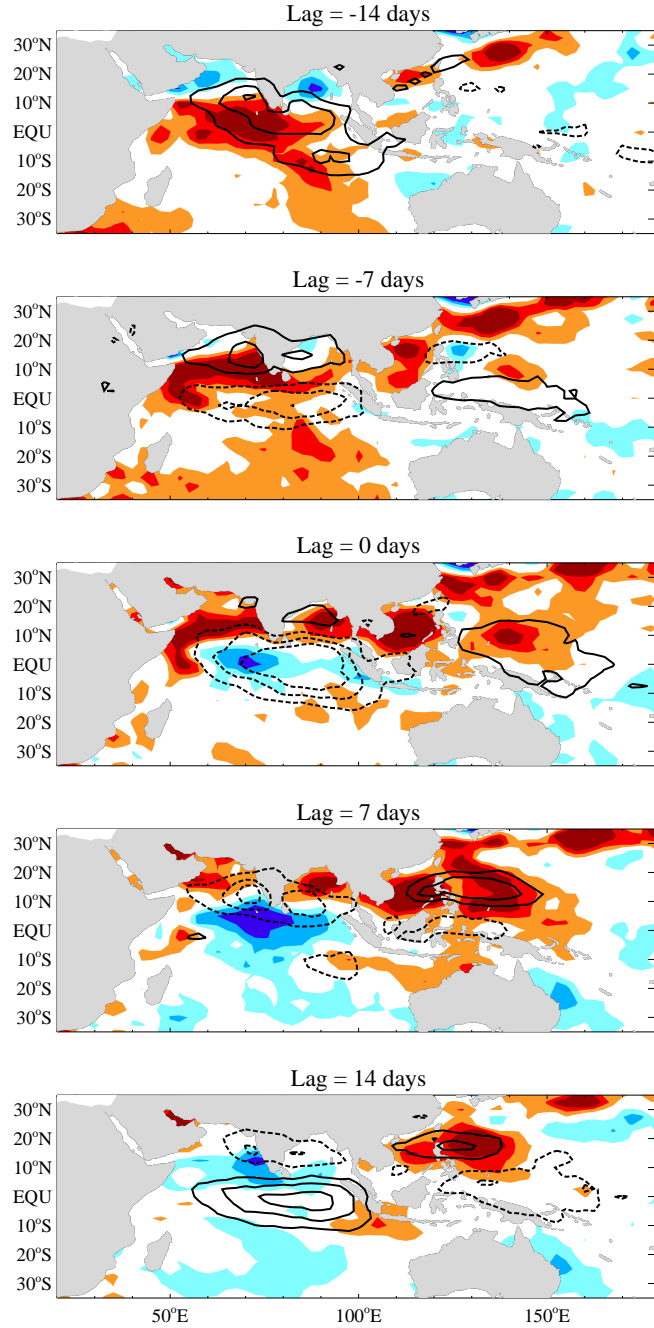


Figure 3.20. Lagged SST anomaly (shaded) and OLR<sub>25–80</sub> (contours) composite maps for SN events. Composite includes the 15 SN events in the 1982–1997 summers. SST anomaly contour intervals are every 0.04°C with red colors indicating positive SST anomalies and blue colors indicating negative SST anomalies. OLR contour intervals are every 7.5W m<sup>-2</sup>, solid contours indicate positive anomalies and dashed contours indicate negative anomalies.

both a reduced latent heat flux out of the ocean as well as diminished upwelling of cold sub-surface water along the northeast African coast. Both factors would yield warmer SSTs. By day +14 the convection is centered over peninsular India and cool SST anomalies are seen along  $0^{\circ}$ – $10^{\circ}$ N. Figure 3.21 shows lag-latitude and lag-longitude diagrams of the composite SST anomalies and OLR<sub>25–80</sub> along  $85^{\circ}$ – $90^{\circ}$ E and  $5^{\circ}$ S– $5^{\circ}$ N. The SST anomalies trail the convection anomalies by a one-quarter cycle along both the latitudinal and longitudinal axis. The largest SST anomalies occur in the northern Bay of Bengal which is characterized by a shallow fresh mixed layer due to heavy rainfall and river inflow. Consequently, small changes in surface heat flux may readily generate detectable SST variations. Interestingly, a composite based on EN events, which typically occur later in the monsoon season, does not show such clear and coherent variations in SST. One possible explanation for this is that, as the strong and steady southwesterly monsoonal surface winds stir up the ocean throughout the season, the mixed layer in the Bay of Bengal deepens, thus making the SST less susceptible to small changes in surface heat flux introduced by the passing of an ISO. It is important to note that because the composites reported here include only 15 events each, the results can not be considered definitive, but they are suggestive nonetheless.

### 3.5 Summary and Discussion

Perhaps the most important result in this chapter is that the northern summer ISO displays similar characteristics to its wintertime counterpart. The resemblance to a Kelvin-Rossby wave response to equatorial heating is apparent in the circulation patterns at both upper and lower levels during both the summer and winter seasons. Surface frictional convergence into the low pressure regions at the center

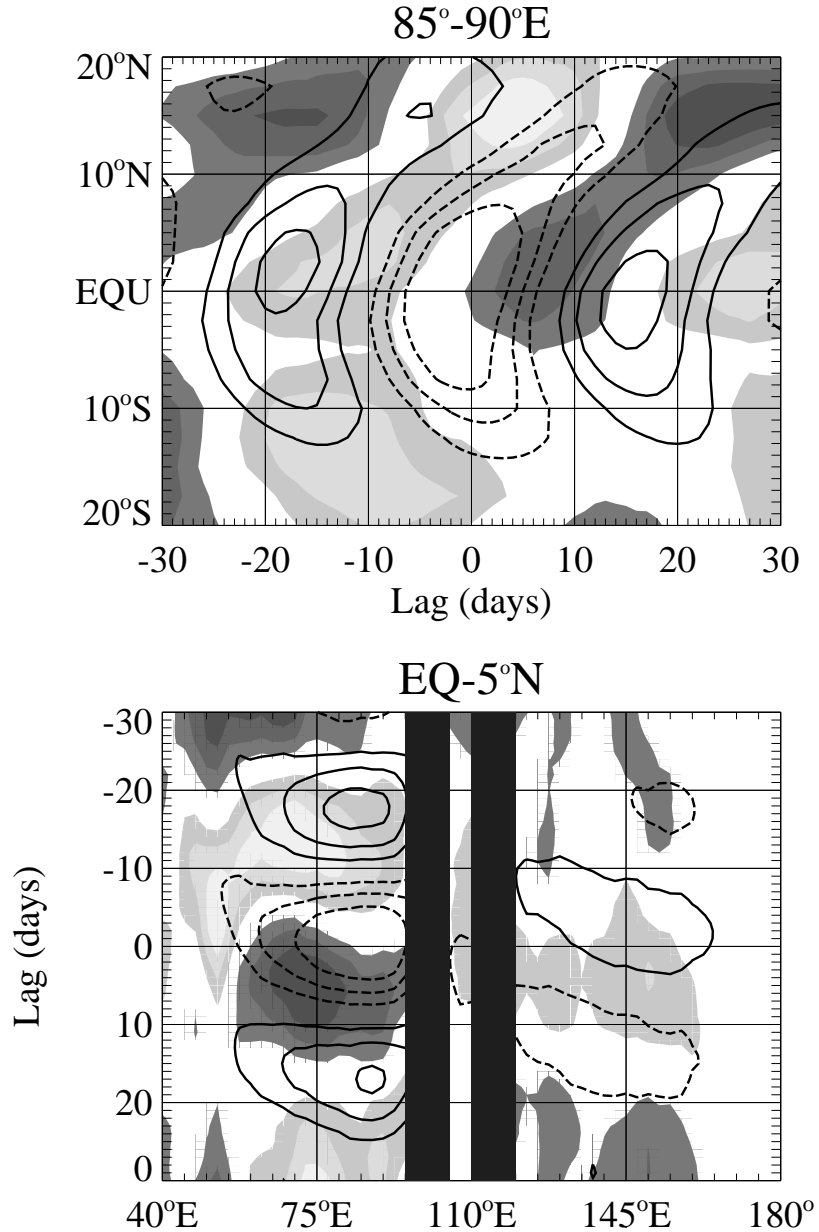


Figure 3.21. Lag-latitude and lag-longitude diagrams of SST anomaly (shaded) and  $\text{OLR}_{25-80}$  (contour). Contour intervals every  $0.04^{\circ}\text{C}$  with the zero contour omitted. Light shades are positive SST anomalies and dark shades are negative SST anomalies. OLR contours every  $7.5 \text{ W m}^{-2}$  with the zero contour omitted. Solid contours indicate positive OLR anomalies and dashed contours indicate negative OLR anomalies. Longitudes that are not over water between the equator and  $5^{\circ}\text{N}$  are marked by the gray columns.

of the Rossby cells is apparent in both seasons, although the strength of the convergence is asymmetric towards the summer hemisphere. The asymmetry of the Rossby cell surface convergence across the hemispheres (Figs. 3.9 and 3.11) is generated by cross-equatorial surface flow into the summer hemisphere that is forced by the slight displacement of the strongest equatorial convection and hence the strongest equatorial heating into the summer hemisphere.

During summer, when the entire Indian Ocean basin exhibits SSTs in excess of 28°C and the boundary layer is very moist, the off-equatorial surface convergence into the Rossby cell generates deep off-equatorial convection which appears as a band of convection that stretches from the equator northwestward to about 20°N (Fig. 3.7). The eastward progression of the northwestward oriented band of convection across the Indian Ocean basin yields an apparent northward propagation along an individual longitude line as well as an eastward propagation along an individual latitude line.

It is important to stress that the results summarized here represent a mean evolution of an ISO. Examination of individual ISO events reveals a large degree of variability in both the evolution of the large-scale convection and the associated circulation patterns. For example, some ISOs do not exhibit a continuous northwestward oriented band of convection from the equator to 20°N. Instead, there is often a clear separation between the equatorial convection and the off-equatorial convection. Such a separation can create the illusion of a pulsing on and off of convection between the equatorial Indian Ocean and India.

Webster *et al.* (1998) suggest that transitions between active and break periods may be chaotic. While an orderly transition between an active and break period can be charted through the statistical techniques used here, in reality, the

summer ISO does not exhibit regular periodicity. One would anticipate that the predictability of the ISO, and therefore forecasts of active and break periods, would be poorer during summer relative to the winter and spring. Additionally, as will be shown in Chapter 4, during some years there is reduced summer ISO activity and that, during those years, active and break periods are less well defined and the transitions between active and break periods are not as coherent.

Wang and Rui (1990) identify a summertime mode that is described as an independent northward moving event. Evidence of such a type of event is not found here, although it does appear that particularly the SN events are characterized by the absence of a strong convection anomaly over the maritime continent between 100° and 120°E. The appearance of a weak convection anomaly over the maritime continent is consistent with the findings of Weickmann and Khalsa (1990) who showed that the ISO signal in convection is generally weak over the maritime continent relative to the Indian and western Pacific Oceans.

The SN and EN modes do not appear to be driven by different dynamics. Instead, the SN and EN modes appear as the two predominantly encountered manifestations of the evolution of the ISO convective component. Both modes exhibit the characteristics of convection coupled to a Kelvin-Rossby wave packet that moves steadily eastward, but the two modes differ in how the convection in the central Indian Ocean develops prior to the mature development of the Kelvin-Rossby wave packet. One possible factor, suggested by this study, determining the two forms of evolution of convection is the different underlying base states. SN events are more commonly encountered during the beginning of the monsoon season, when the SSTs are at a maximum, whereas EN events typically occur later in the season after the SSTs have cooled somewhat. These observations led to the speculation that the SST

distribution across the equatorial Indian Ocean basin is a primary factor determining the form of the summertime ISO evolution.

A more complete understanding of the evolution of the two ISO modes may lead to better empirical prediction of the timing of upcoming active and break periods. For example, the appearance of a large scale envelop of convection in the central equatorial Indian Ocean signals the start of an active period over central peninsular India ( $15^{\circ}\text{N}$ ,  $75^{\circ}\text{E}$ ) within about 12–16 days if the equatorial convection exhibits predominantly eastward character and 16–20 days if it exhibits primarily stationary behavior.